JGR Planets

RESEARCH ARTICLE
10.1029/2021JE006942

Key Points:

- Fe_3S is not present under sufficiently hydrogen-rich conditions, being replaced by FeH_x and FeS or FeS_xH_y and FeH_x
- At 23–35 GPa, separate FeS and FeH_x phases exist stably, whereas above 35 GPa, a new Fe alloy phase appears, which may contain both S and H
- Crystallization from an Fe-S-H liquid would lead to a complex core structure

Supporting Information:

Supporting Information may be found in the online version of this article.

Correspondence to:

H. Piet and S.-H. Shim,
helene.m.piet@gmail.com;
sshim5@asu.edu

Citation:

Piet, H., Leinenweber, K., Greenberg, E., Prakapenka, V. B., & Shim, S.-H. (2021). Effects of hydrogen on the phase relations in Fe-FeS at pressures of Mars-sized bodies. *Journal of Geophysical Research: Planets*, *126*, e2021JE006942. https://doi.org/10.1029/2021JE006942

Received 5 MAY 2021
Accepted 21 OCT 2021

Effects of Hydrogen on the Phase Relations in Fe-FeS at Pressures of Mars-Sized Bodies

H. Piet[1], K. Leinenweber[2], E. Greenberg[3], V. B. Prakapenka[3], and S.-H. Shim[1]

[1]School of Earth and Space Exploration, Arizona State University, Tempe, AZ, USA, [2]School of Molecular Sciences, Arizona State University, Tempe, AZ, USA, [3]GeoSoilEnviroCars, University of Chicago, Chicago, IL, USA

Abstract The large radius, and therefore low density, of the Martian core found in the InSight mission data analysis highlights the importance of considering other light elements besides sulfur (S), which has been considered as the main light element for Mars for decades. Hydrogen (H) is abundant in the solar system and becomes siderophile at high pressures. Although Fe-S and Fe-H systems have been studied individually, the Fe-S-H ternary system has only been investigated up to 16 GPa and 1723 K. We have investigated the Fe-S-H system at pressures and temperatures (*P-T*) relevant to the cores of Mars-sized planets (up to 45 GPa and well above the melting temperature of FeS) in the laser-heated diamond anvil cell combined with in situ synchrotron X-ray diffraction. We found that sufficient hydrogen leads to the disappearance of Fe_3S at high *P-T*. Instead, separate Fe-H and Fe-S phases appear at 23–35 GPa. At pressures above 35 GPa, we found a new phase appearing while Fe-S phases disappear and Fe-H phases remain. Our analysis indicates that the new phase likely contains both S and H in the crystal structure (tentatively FeS_xH_y where $x \approx 1$ and $y \approx 1$). The observed pressure-dependent changes in the phase relation may be important for understanding the structure and dynamics of the Martian core and the cores of Mars-sized exoplanets.

Plain Language Summary The metallic cores of planets and satellites are believed to contain significant amounts of light elements such as hydrogen and sulfur. To understand how a planetary core forms and evolves through time, it is important to know how iron alloys behave at the pressure-temperature conditions of the cores. The iron-hydrogen and the iron-sulfur alloy systems are well-known even at the Earth's core conditions. However, the iron alloy systems with both sulfur and hydrogen together have been studied only for depths of smaller bodies like Ganymede. Using new experimental techniques, we study the behavior of the iron-hydrogen-sulfur alloy system at higher pressures and temperatures. We found that at intermediate depths, sulfur and hydrogen form two separate iron alloys, while at greater depths, a new iron alloy with both sulfur and hydrogen may form in the cores of Mars-sized planets. This change in mineralogy with depth, therefore, suggests that the structure and dynamics in the cores of Mars-sized planets could be much more complex if hydrogen can be added to the region as a light element.

1. Introduction

Significant amounts of light elements are necessary to explain the observed density deficit of the Earth's core from a pure Fe-Ni alloy (Birch, 1952). Silicon, sulfur, oxygen, carbon, and hydrogen are strong candidates to lower the core's density because of their cosmochemical abundances and affinity with metallic iron at high pressures and temperatures during core formation (Poirier, 1994; Wade & Wood, 2005). Although a combination of light elements is more likely to explain the density deficit than just one element, a consensus on the combination itself has yet to be reached (Badro et al., 2014).

For Mars, recent InSight SEIS data analysis found a much greater radius of the core than previously believed, suggesting a much lower density and therefore much larger amounts of light elements (Stähler et al., 2021). The study also found that the required amount of S to explain the large core size exceeds the cosmochemically estimated amount of S in the Martian core. Therefore, the role of other light elements would be important.

Sulfur (S) and hydrogen (H) were both abundantly available in the proto-planetary disk from which planets and satellites in the solar system formed. Although S and H are both volatile elements at 1 bar, they show

siderophile (iron-loving) behaviors at pressures relevant to core formation processes (Badding et al., 1991; Li & Agee, 2001; Pépin et al., 2014). Fe-S and Fe-H systems, separately, have been extensively studied (e.g., Badding et al., 1991; Fei et al., 1995; Kamada et al., 2010; Pépin et al., 2014; Stewart et al., 2007). Experiments have shown that the solubility of H into metallic Fe increases significantly with increasing pressure (Badding et al., 1991; Pépin et al., 2014) up to FeH_5 (Pépin et al., 2017). The Fe-FeS system is eutectic up to 271 GPa, where Fe_3S is stable together with pure Fe (Ozawa et al., 2013; Stewart et al., 2007). Both sulfur and hydrogen have been shown to significantly lower the melting temperature of pure Fe (Fei et al., 1995; Hirose et al., 2019; Kamada et al., 2010; Morard et al., 2007; Sakamaki et al., 2009). Low melting temperatures (like those of Fe_3S and FeH) could, for example, increase the longevity of a liquid core and therefore contribute to the dynamics of the region. Additionally, recent experiments underline the important effects of S and H on the density and sound velocities of iron alloys at the pressure conditions relevant to the cores of Mars-sized planets (Nishida et al., 2020; Thompson et al., 2018). S and H should therefore have important implications for planetary cores. A study up to 16 GPa reported the solubility of H into FeS, thus forming a $FeSH_x$ phase (where $x \approx 0.3$) (Shibazaki et al., 2011). However, the behavior of the Fe-S-H system is unknown beyond these conditions.

Because H is very volatile and highly reactive, it is a challenging element to study at high pressures and high temperatures. A few studies have investigated phase relations for hydrogen-involved ternary systems. Narygina et al. (2011) and Ohta et al. (2019) have shown that when pure Fe reacts with paraffin (C_nH_{2n+2}, $n > 5$) up to 68 GPa, FeC and FeH form separate solid phases under subsolidus conditions. Hirose et al. (2019) also showed that up to 127 GPa at liquidus conditions, H preferentially partitions into the liquid, thus limiting the solubility of C in the liquid. Ohtani et al. (2005) observed the formation of separate FeO and FeH phases when Fe reacts with H_2O below 84 GPa, whereas above 78 GPa, the coexistence of FeOOH and FeH_x was observed (Liu et al., 2017; Yuan et al., 2018). On the other hand, H does not seem to alter the compressibility of hcp FeSi or induce any phase separation like that observed for Fe-C and Fe-O systems (Tagawa et al., 2016).

The co-solubility of H with another light element in iron alloy appears to be a complex variable of pressure, temperature, and composition (e.g., Tagawa et al., 2016). It is therefore difficult to interpolate the geophysical implications of a ternary system from separate binary systems given the seemingly complex relationships between light elements. Whether it is by experimental design or not, studies using impure H sources must consider the potential effects of other elements, such as C in the case of paraffin or oxidized conditions in the case of H_2O. While more ideal from a compositional point of view, the use of a pure H_2 source comes with its own set of experimental challenges: the high mobility and diffusivity of H at high *P-T* make diamond anvils much more brittle: therefore, increasing the chance for experiment failure when a H medium is combined with conventional continuous wave laser heating in the diamond-anvil cell (DAC). Regardless, pure H_2 medium is the most ideal H source when studying the effect of H on any system, and recent experimental progress with the advent of pulse laser-heating systems (Deemyad et al., 2005) combined with time-gated X-ray diffraction (XRD) (Goncharov et al., 2010) now allow significant reduction of diamond embrittlement during experiments with pure H, while still providing XRD patterns.

We have conducted experiments on phase relations in the Fe-S-H system at pressures up to 45 GPa and temperatures above the liquidus of FeS, using laser-heated diamond-anvil cells combined with synchrotron X-ray diffraction for in situ high pressure and high temperature phase characterization. We then discuss the potential implications of our experimental observations for the crystallization of cores of Mars-sized planetary bodies.

2. Experimental Methods

2.1. Starting Materials

The pure Fe_3S sample was synthesized in a 1,100 ton multi-anvil press at ASU following the methodology of Kamada, Ohtani, Fukui, et al. (2014). A Fe + FeS mixture was loaded in an MgO capsule and pressurized to 21 GPa using an 8/3 cell assembly (Leinenweber et al., 2012). Heating was conducted in three stages: 5 min at 1533 K for melting and homogenization of the mixture, then 30 min at 1413 K to favor the crystallization of Fe_3S grains, and finally 1 hr at 1273 K to enhance the growth of Fe_3S grains. The sample was then quenched to room temperature and progressively brought back to room pressure overnight.

Energy-dispersive spectroscopy chemical mapping in scattering electron microscopy (SEM) and XRD data were acquired after recovery to examine the chemical composition and crystal structure of synthesized crystals, respectively (see Figure S1 and Table S1 in Supporting Information S1), and confirmed the purity and homogeneity of the sample.

We also explored other compositions along the Fe-FeS join: Fe + Fe_3S mixture and FeS. FeS was obtained from Alfa Aesar (ACS: 1317-37-9, lot # 22388-06) chemicals. Ferrous sulfide is often slightly iron deficient, $Fe_{1-\delta}S$, and therefore nonstoichiometric. For the Fe + Fe_3S, we used a mixture of Fe metal and Fe_3S. Since only small amounts of multi-anvil samples were available, the mixture was not sufficiently homogeneous for maintaining the same compositions for diamond-anvil cell loadings. Therefore, we used the mixture data only to qualitatively supplement our main data from Fe_3S.

2.2. Diamond-Anvil Cell Preparation

Pressures were achieved using diamond anvils ranging in size from 200 to 150 μm. We loaded a thin foil of the starting material (5 μm in thickness and 50–70 μm in diameter) into pre-indented and drilled rhenium gaskets (18–20 μm in thickness for the indentation and 70% of the cullet size for the diameter of the sample chamber). The rhenium gaskets were gold-coated to reduce the diffusion of hydrogen into the gasket material, which can weaken the gasket and therefore result in anvil failure (Pépin et al., 2014). To ensure proper insulation from the diamonds during laser-heating, we propped the sample using small pieces of the same starting material. We used gold as a pressure marker (Ye et al., 2017). To prevent unwanted/unknown reactions between gold, hydrogen, and the sample during high-temperature experiments, we chose not to mix gold with the sample but instead load it as a separate chip next to the sample. We then loaded pure hydrogen gas at a pressure of 1,500 bar into the sample chamber using the hydrogen gas loading facility located at Arizona State University. After the gas loading, we compressed the cell to its target pressure. In-house monitoring of pressure after hydrogen loading was enabled by the presence of a small ruby chip placed in the sample chamber prior to hydrogen loading (Mao et al., 1986).

2.3. Synchrotron Measurements

Synchrotron X-ray diffraction (XRD) experiments were performed at in situ high-pressure and high-temperature in the laser-heated diamond anvil cell. The experiments were conducted at the 13-IDD beamline of the GSECARS sector of the Advanced Photon Source. We focused a monochromatic X-ray beam with an energy of 30 keV or 37 keV on the sample and align it coaxially with double-sided near-infrared laser-heating beam. The laser-heating spots have a 25- μm diameter. The X-ray beam size was 3×4 μm^2. We used the pulsed laser-heating technique to prevent significant anvil embrittlement enhanced by hydrogen during laser heating (Deemyad et al., 2005). For this, the laser pulse was synchronized with gated X-ray to allow for the acquisition of diffraction patterns at in situ high *P-T* (Goncharov et al., 2010). For high quality diffraction patterns, we accumulated 10^5 pulse heating + XRD events with a repetition rate of 10 kHz. For measurements at 300 K, we used regular continuous-wave (CW) mode for higher quality (Prakapenka et al., 2008).

Short heating aspects of the pulsed laser technique were considered in the data analysis. At the high temperatures of our study, hydrogen should be liquid (Deemyad & Silvera, 2008) and therefore its diffusion into metal is very fast, for example $\sim 10^3$ $\mu m^2/s$ at low pressures (Zhang et al., 2008). Given the small grain size (≤ 1 μm) of the metal sample foils made from cold compression of powder starting materials, typical of LHDAC loading, hydrogen diffusion from the grain boundary during laser heating could allow sufficient conditions for complete reaction for accumulated heating of ~1 s performed in our experiments.

X-ray diffraction images were measured using a Pilatus 1M CdTe detector. We used a LaB_6 standard to calibrate and correct distortions and detector distance (~200 mm) for the integration of diffraction images to 1D diffraction patterns in the Dioptas software (Prescher & Prakapenka, 2015). We used the PeakPo software package for peak identification and unit-cell fitting (Shim, 2017).

The temperature was calculated by fitting the thermal radiation spectra to a Planck equation assuming a gray-body approximation (Prakapenka et al., 2008). We obtained temperatures for both sides of DAC. As

discussed above, because a separate gold grain was loaded instead of mixing with the sample to avoid any possible alloying between gold and Fe-S, pressure could not be directly measured during heating. Therefore, we assigned pressures measured before and after heating for high temperature data points. A previous calculation showed that thermal pressure is 0.5–2.5 GPa at 1000–4000 K, assuming a liquid state of an Ar medium (Dewaele et al., 1998). In our experiments, the H medium adjacent to the heating spot would be molten during heating considering its low melting temperature (Deemyad & Silvera, 2008). Therefore, we assigned 10% uncertainties for the pressures of high temperature data points.

2.4. Electron Probe Micro Analysis

To resolve chemical compositions of the phases synthesized at high *P-T*, electron probe micro-analysis (EPMA) was performed on starting materials synthesized in the multi-anvil press and on the recovered samples from the laser-heated diamond-anvil cell (LHDAC). X-ray intensity mapping and semi-quantitative point analysis were performed at Arizona State University's Eyring Materials Center using a JEOL JXA-8530F. To avoid charge buildup, samples were coated with a thin conductive C-layer to increase electron conductivity and improve sample imaging and analysis. Sample imaging was mainly done using back-scattered electrons (BSE). For energy dispersive spectroscopy (EDS) X-ray intensity mapping, the electron microprobe was operated at 20 kV with a current of 75 nA and a dwell time of 50 ms, producing 128 × 96 pixel maps. For wavelength dispersive spectroscopy (WDS) X-ray intensity mapping, the microprobe was operated at 20 kV with a current of 100 nA and a dwelling time of 50 ms, resulting in 270 × 270 pixel maps.

Considering the beam penetration and the depth of electron interaction combined with small grain sizes of the phases from LHDAC experiments, EPMA could sample signal from underlying phases. This problem could have been reduced by making thin sections at the laser-heated spots using a focused ion beam (FIB). However, the many samples were lost during laser heating because of failure of diamond anvils by hydrogen-induced embrittlement. For the case where we were able to decompress to 1 bar for recovery, the gasket hole was often completely collapsed, leading to crushing of the sample foils. The sample chamber collapse is unusually frequent compared with other more rigid media, which is likely because of high compressibility of hydrogen and/or sudden escape of hydrogen when it coverts from solid to liquid and then gas during decompression.

A few sample foils that survived in a less-collapsed sample chamber were found to have severe development of microcracks (Figure S2 in Supporting Information S1). Such a change is likely related to a hydrogen medium combined with laser heating because the sample foils were produced by cold compression to a few GPa of pressures, which typically reduce such cracks in malleable alloys but do not remove them completely. Because of this, the foils were very fragile, and therefore, lift from the chamber can often crumble into powder. For these reasons, we chose EPMA, which requires minimal processing of the mechanically weakened recovered samples.

3. Results and Discussion

3.1. Fe_3S + H

We investigated the reaction between Fe_3S and pure hydrogen at pressures of 23–45 GPa and temperatures up to 4000 K. In all the runs, no reaction of Fe_3S with hydrogen was observed under cold compression to high pressures (i.e., before laser heating) (Figure 1a), and the measured unit-cell volume of the phase is consistent with that of pure Fe_3S reported at the same conditions (Fei et al., 2000). Therefore, we interpret that Fe_3S does not react with hydrogen at room temperature and high pressures. The behavior is in contrast with that of pure Fe metal at similar pressures: Fe metal reacts with hydrogen at 300 K and converts to a double hexagonal close-packed (dhcp) structure of FeH_x (Badding et al., 1991). Our measured volumes for the dhcp phase (also for fcc phase, which will be discussed later) agree well with previous reports (Narygina et al., 2011; Pépin et al., 2014) where x in FeH_x is found to be close to 1 based on the unit-cell volume expansion (Figure S3b in Supporting Information S1). While such an estimation remains indirect and therefore, x may not be exactly 1; in this paper, we use FeH specifically for the discussions on the FeH_x phases with x values close to 1 based on the estimation from volume expansions in previous studies.

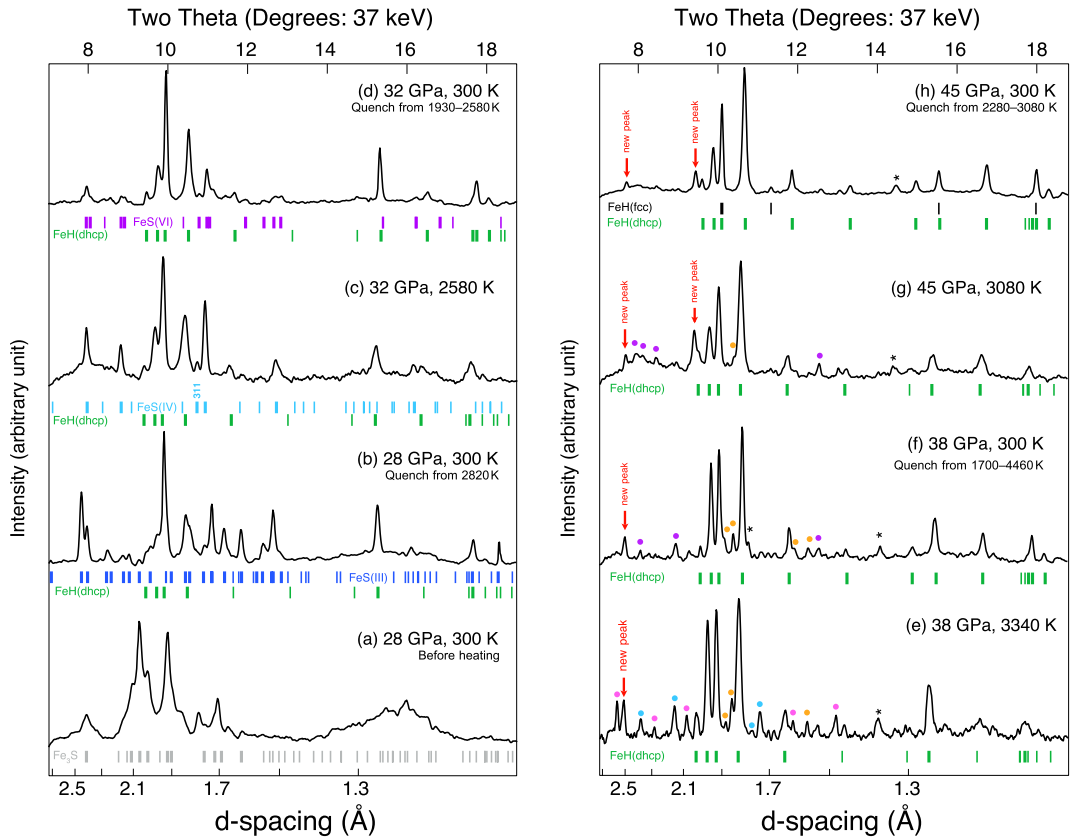

Figure 1. X-ray diffraction for runs starting with $Fe_3S + H_2$. The thin vertical ticks show all the expected *d*-spacing and intensity for a given phase and the thick vertical ticks highlight the observed ones. The colored dots highlight observed peaks from minor phases (orange: Fe_2S; purple: FeS(VI); cyan: FeS(IV); pink: FeS_2). Unidentified peaks are indicated by *. (a) Fe_3S starting material before heating. (b) Formation of dhcp FeH_x, FeS(VI) and FeH_2 after laser heating of Fe_3S in a H medium (temperature quench). (c) Formation of dhcp FeH_x and FeS(IV) observed during in situ heating at 32 GPa. (d) FeS(VI) and dhcp FeH_x formed from FeS(IV) + H after laser heating (temperature quench). (e) Formation of dhcp FeH_x, FeS(IV), and FeS_2 from Fe_3S + H of during heating at 38 GPa. New peaks (red arrows) appear at > 38 GPa. (f) Appearance of new peaks with dhcp FeH_x and FeS(VI) after laser heating (temperature quench). (g) Formation of dhcp FeH_x, FeS(VI), and a new phase from Fe_3S + H during laser heating. (h) dhcp FeH_x, FeS(VI), and the new peaks observed after temperature quench. The volume of the dhcp is close to $x \approx 1$ in FeH_x based on the unit-cell volume (see text for more information).

After a Fe_3S sample was heated in a H medium to 2830 K at 28 GPa, the phase completely disappeared from the diffraction patterns (Figure 1b). The instability of Fe_3S at 28 GPa is striking since Fe_3S is reported to be stable up to 271 GPa at 3300 K (Ozawa et al., 2013) This observation shows that the behavior of Fe_3S is fundamentally different when sufficient H is present in the system. In the place of Fe_3S at 28 GPa, after laser heating we observed a mixture of dhcp FeH and FeS(III), indicating that there is a stable tie-line between these two phases instead of between Fe_3S and H. The measured unit-cell volume of dhcp FeH_x is similar to what is expected for $x \approx 1$ at 28 GPa (Pépin et al., 2014). FeS(III) has a noticeably greater unit-cell volume than reported at this pressure (Kusaba et al., 1997) (Figure S3 in Supporting Information S1), suggesting the incorporation of H into the FeS(III) structure. The heating temperature, 2820 K, at 28 GPa is above the melting temperatures of FeS (Boehler, 1992) and FeH_x (Sakamaki et al., 2009), and the eutectic temperature of Fe-Fe_3S (Kamada et al., 2010) (Figure 2a). Therefore, we interpret that Fe_3S melted and reacted with a H medium, forming an Fe-S-H liquid. Then the observed FeS and FeH phases are the crystallization products of the Fe-S-H liquid. At 32 GPa, the same trend continues: disappearance of Fe_3S and appearance of dhcp FeH and FeS (Figures 1c and 1d) upon heating. Again, here the heating temperatures are higher than the expected melting temperatures of FeS and FeH_x.

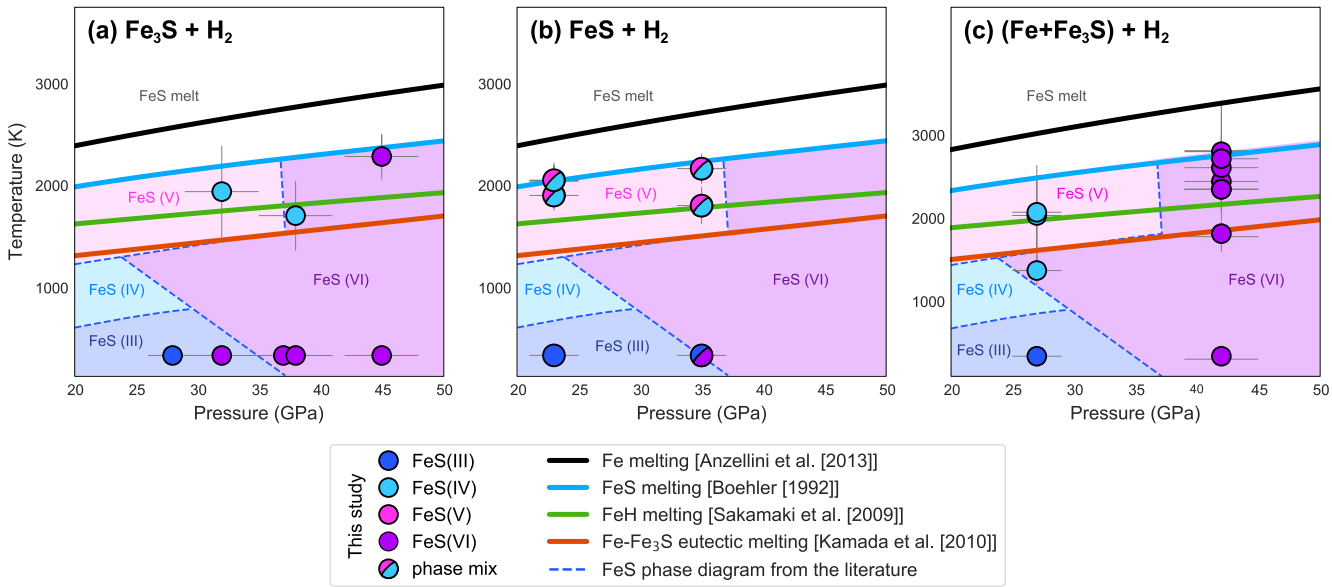

Figure 2. Pressure-temperature conditions for the observations of different polymorphs of FeS in a hydrogen medium in: (a) $Fe_3S + H_2$, (b) $FeS + H_2$, and (c) $(Fe + Fe_3S) + H_2$ starting materials. In this figure, we show only the data points measured below FeS melting. We also have some other data points measured above melting temperatures of iron alloys (Table S2 in Supporting Information S1). The symbol colors refer to the observed polymorphs of FeS at the conditions (see legend). The reported polymorphs at 300 K are those observed after temperature quench. The solid lines represent the melting curves of different phases: black: pure Fe (Anzellini et al., 2013); blue: FeS (Boehler, 1992); green: FeH_x (Sakamaki et al., 2009); and orange: eutectic for Fe–Fe_3S (Kamada et al., 2010). For comparison, we present stability fields and boundaries for FeS polymorphs in H-free system (Fei et al., 1995; Kavner et al., 2001; Ohfuji et al., 2007; Ono & Kikegawa, 2006; Urakawa et al., 2004).

FeS(IV) and its higher temperature polymorph FeS(V) both feature NiAs-type structures, resulting in very similar diffraction patterns (Figure 2a). The observation of FeS(IV) instead of FeS(V) above 1900 K (by the diagnostic 311 peak; Figure 1c) is discrepant from reports for H-free FeS in the literature (Fei et al., 1995; Kavner et al., 2001; Ohfuji et al., 2007; Urakawa et al., 2004). The measured unit-cell volumes of FeS(IV) are somewhat higher than expected at 32 GPa (Urakawa et al., 2004) (Figure S3 in Supporting Information S1), which indicates that a small amount of H could stabilize FeS(IV) over FeS(V). Upon quench, FeS(IV) transforms to FeS(VI) (Figure 1d), whereas in H-free systems, FeS(IV) was instead observed to transform to FeS(III) upon temperature quench (Fei et al., 1995; Ohfuji et al., 2007; Urakawa et al., 2004). Ohfuji et al. (2007) did observe that FeS(IV) transforms to FeS(VI) with heating above 1300 K, but here the transition is observed upon temperature quench and could be an effect of H. Therefore, while a majority of H is alloyed in Fe metal to form FeH_x when Fe_3S liquid crystallizes, some small amounts of H alloy with FeS phase and affect the phase behaviors.

At 38 GPa, unlike the results at lower pressures, we find a new peak appearing during heating at $d_{sp} = 2.87$ Å, which will be discussed later. A few weak diffraction peaks also appear during or after heating. Although they can be assigned to either FeS_2 or *Pnma*-Fe_2S (Zurkowski, 2020), because these peaks are mainly from weak spots in diffraction images, their assignments are not conclusive. Given the low intensity of these phases, they are likely related to thermal gradients during laser heating. Therefore, we interpret that they are not stable phases at the *P-T* conditions with hydrogen.

At 45 GPa and 3080 K, Fe_3S reacts with hydrogen and completely transforms into dhcp FeH and FeS(VI) (Figure 1g). The previously observed new peak is again present here, as well as an additional strong new peak ($d_{sp} = 2.24$ Å). Weak peaks, which can be assigned to FeS_2 progressively disappear with further heating in the 2280–2590 K range, regardless of temperature, and could be caused by thermal heterogeneity during laser heating. Similarly, intensities of the peaks, which can be assigned to FeS(VI) and Fe_2S decrease with further heating, and Fe_2S has completely disappeared with temperature quench. Dhcp FeH and the new peaks, however, grow stronger with subsequent heating and remain the major phases in the final quench (Figure 1h). The stronger than expected intensity of the 004 dhcp FeH peak ($d_{sp} = 2.05$ Å at this pressure) in the pattern suggests that the observed peak intensity does not only result from the presence of dhcp FeH.

A legitimate candidate to explain the observation is fcc FeH_x, which has been reported to form at high temperature at this pressure range (Kato et al., 2020; Thompson et al., 2018), and which 111 peak could account for the observed intensity.

3.2. FeS + H

To further understand the phase behavior of Fe-S-H system, we also studied the $Fe_{1-\delta}S$ starting material in a hydrogen medium using the same experimental procedure as for Fe_3S + H at similar pressures. Before heating at 23 GPa, the pattern can be explained by a single FeS(III) phase. The measured unit-cell volume of the phase is slightly higher than that of pure FeS(III) at the same pressure (Figure S3 in Supporting Information S1) (Kusaba et al., 1997), suggesting some solubility of H in this FeS(III) phase even without heating. With heating, fcc FeH appears in diffraction patterns as a major phase. Some minor peaks can also be assigned to dhcp FeH (Figure 3b). Dhcp FeH was observed to be a more prominent phase in runs starting with Fe_3S. Although we do not have direct evidence for this, the prominence of fcc FeH over dhcp FeH in FeS + H_2 runs suggests that some S in the crystal structure may affect the stability of one structure with respect to another since the S content is the most notable difference between the Fe_3S + H_2 runs and the FeS + H_2 runs.

We also identify both FeS(IV) and FeS(V) at high temperature (Figure 2b). FeS(V) was not observed in runs with the Fe_3S + H starting materials. Since FeS(V) is usually the stable polymorph at these *P-T* conditions in H-free systems (Ono & Kikegawa, 2006), we attribute the existence of both FeS(IV) and FeS(V) to an incomplete reaction of FeS with H where FeS(IV) results from the reaction with H at high temperature and FeS(V) is the non-reactive FeS phase. The absence of volume change from its expected volume at 23 GPa is also a good indicator that the phase did not react with hydrogen (Figure S3 in Supporting Information S1). Upon temperature quench, both FeS phases transform to FeS(III) (Figure 3b). The unit-cell volume for FeS(III) being higher than before heating (Kusaba et al., 1997) suggests increased solubility of H in FeS(III) from laser heating.

At 35 GPa and 3674 K, FeS(III) in a pure hydrogen medium transforms to a FeS(IV)-FeS(V) mixture similar to what is observed at 23 GPa. There are, however, a few important differences between the runs at 23 GPa and the one at 35 GPa. First, we found more enhanced diffraction intensities from dhcp FeH_x (Figure 3c). The difference in behavior might be related to extremely high temperature above melting achieved in this higher pressure run. Second, we observed the same new peaks found in Fe_3S + H runs. The number of phases observed in the diffraction pattern exceeds the number expected for thermal equilibrium in Fe-S-H ternary. Because heating was conducted at a temperature much above melting, it is possible that thermal gradients were more severe and therefore result in complex crystallization during temperature quench.

In most of the experiments for the $Fe_{1-\delta}S$ + H_2 starting materials, we observed FeH_x and FeS. The formation of FeH_x without S at lower pressures requires some amount of S either dissolved in the H medium or reacting with H to form an S-H phase. However, S-H phases would be challenging to detect in X-ray diffraction because of very low X-ray scattering cross sections expected for the phases. Therefore, within our resolution, the absence of S-H phase peaks cannot rule out the possibility of its existence in reaction product.

3.3. Fe + Fe_3S + H

Since no Fe-S alloy richer in Fe than Fe_3S exists, we used a mixture of Fe and Fe_3S as a proxy to study how increasing amounts of metallic Fe in the bulk system affects the results when reacted with H (Table S2 in Supporting Information S1). At 27 GPa and 1100 K, we observed fcc FeH_x and FeS(IV). FeS(IV) persisted to higher heating temperatures (up to 2670 K). Again, the presence of FeS(IV) instead of FeS(V) expected at these conditions (Figure 2c), suggests that FeS(IV) might host a significant enough amount of H in order to stabilize the structure at the temperature. At 42 GPa and 2077 K, we observed peaks attributed to the new phase upon heating, which confirms what was observed for pure Fe_3S and FeS starting runs. We also observed FeH_x (mostly in dhcp). Although the existence of multiples of phases in this starting mixture makes the interpretation more complicated, the main features we observed in Fe_3S + H runs and $Fe_{1-\delta}S$ + H runs were reproduced in these experiments.

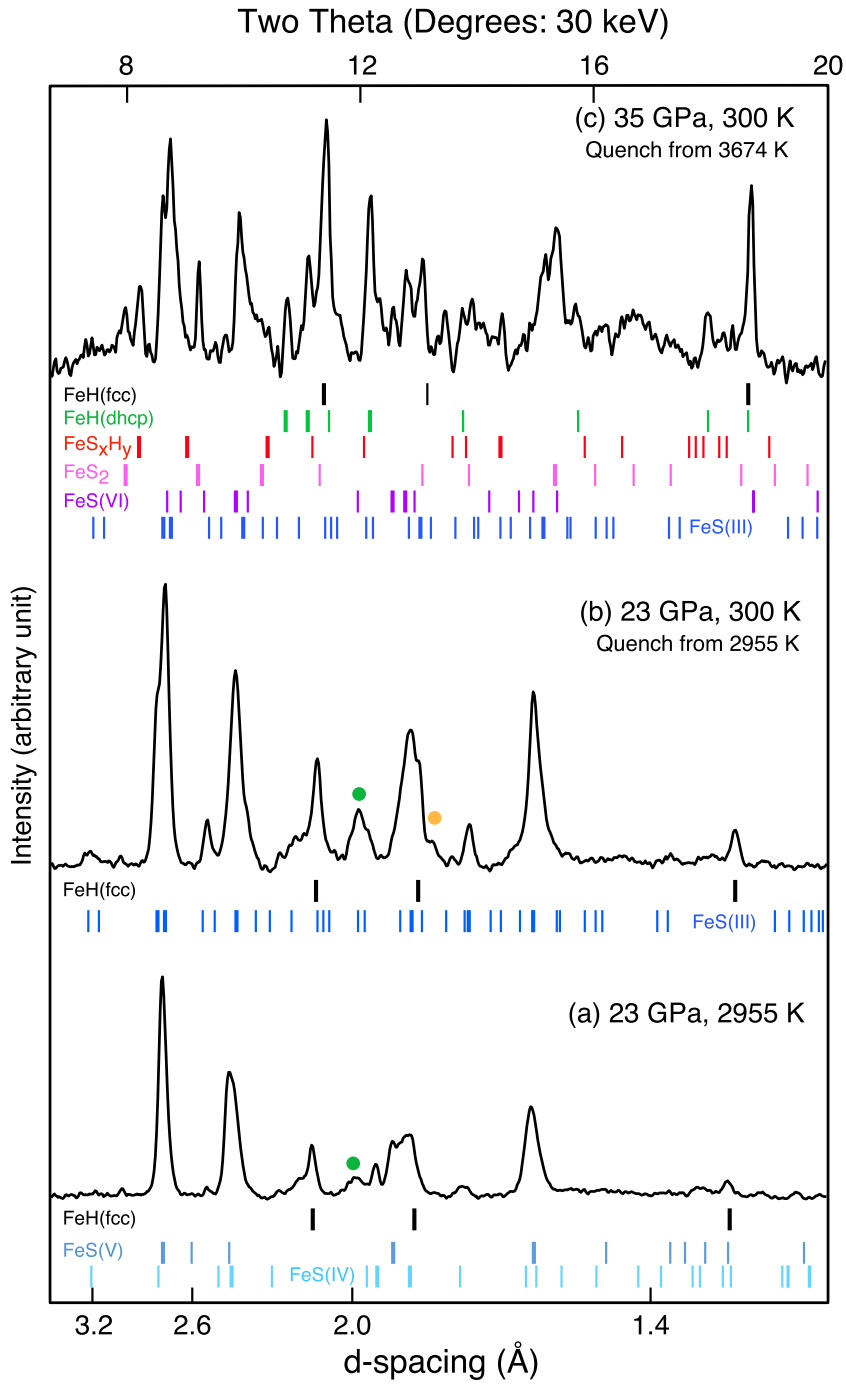

Figure 3. X-ray diffraction for runs starting with $Fe_{1-\delta}S + H_2$. The thin vertical ticks show all the expected *d*-spacing and intensity for a given phase and the thick vertical ticks highlight the observed ones. The colored dots highlight observed peaks from minor phases (green: dhcp FeH_x; orange: Fe_2S). (a) At 23 GPa and 2955 K, fcc FeH_x and FeS(IV) form from the reaction of $Fe_{1-\delta}S$ and H_2, whereas FeS(V) most likely results from non-reactive $Fe_{1-\delta}S$ with H_2. (b) Upon temperature quench FeS transforms entirely to FeS(III). Fcc FeH_x remains a major phase and dhcp FeH_x remains a minor phase. (c) Diffraction pattern measured after temperature quench from 3674 K at 35 GPa is more complex than at 23 GPa. The new phase (FeS_xH_y) is observed, as well as FeS (III and VI), FeS_2 and both fcc FeH_x and dhcp FeH_x are major phases here.

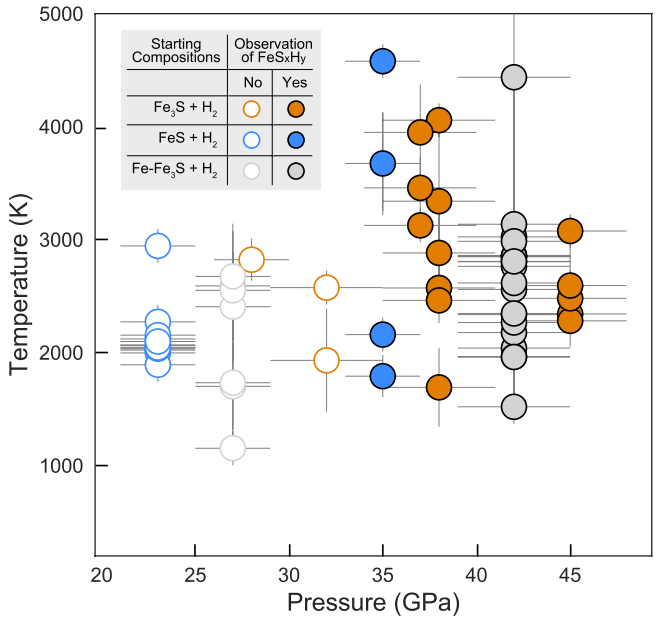

Figure 4. Pressure and temperature conditions for the observation of the new phase associated with the new diffraction peaks. The open and the close circles are for nonobservation and observation of the new phase, respectively. The data points are also presented in Table S3 in Supporting Information S1.

3.4. A New Phase in Fe-S-H

Figure 4 shows the pressure and temperature conditions for all the runs we conducted. In the figure, we highlighted the conditions where the new diffraction lines were observed. The new peaks were observed only above 35 GPa regardless of the starting composition. The stability of the phase does not seem to have a strong temperature dependence either.

Given the presence of Fe-S and Fe-H phases in our runs, a potential candidate to explain the observed new peaks is a counterpart hydrogen sulfide phase. Neither *I*4/*mcm*-H_3S nor *I*222-H_3S, however, provides a match for the observed new peaks in terms of expected peak position or intensity (Duan et al., 2014; Strobel et al., 2011). Although we cannot completely exclude the formation of hydrogen sulfide in our runs, the relatively smaller X-ray scattering cross section of H-S phases compared with iron-bearing phases, would make such a compound challenging to detect and therefore an unlikely source for the intense new lines observed in our diffraction patterns. Regarding the possibility for a Fe-S phase, Shibazaki et al. (2011) reported the formation of $FeSH_x$(IV) and $FeSH_x$(V) at 16.5 GPa and above 800 K. However, volume expanded versions of FeS-(IV) and FeS(V) would only change the peak positions.

The presence of FeH_x in our runs suggests that the new peaks could also be iron hydride. At the investigated *P-T* range, the stable iron-hydrogen alloys are dhcp FeH_x and fcc FeH_x (Badding et al., 1991; Narygina et al., 2011). We found that the observed new lines can be well indexed with a tetragonal unit cell. The positions of all four new peaks can be fit to a FeH_2-like tetragonal structure (Pépin et al., 2014), albeit with an increased unit-cell volume by +60% uniformly along all three directions (Figure 5 and Table S4 in Supporting Information S1). Increased hydrogen solubility in iron hydrides also leads to volume expansion and it was observed for interstitial hydrogen in fcc FeH_x (Narygina et al., 2011) and for hydrogen-to-hydrogen bonded units in FeH_2 and FeH_5 (Pépin et al., 2014, 2017) through the formation of additional layers of hydrogen atoms. However, FeH_5, which was reported to form above 135 GPa (Pépin et al., 2017), does not explain the new peaks (Figure 5). Due to the layered nature of the FeH_2 structure (alternating layers of Fe and H), it is unlikely that more H would explain the observed homogeneous volume expansion to all three directions, but rather would be directional. It is worth noting that FeH_2 was reported to appear only above 67 GPa (Pépin et al., 2014). Therefore, formation of a similar structure at significantly lower pressures requires some other stabilizing sources. Since S can also increase the unit-cell volume, this new phase may contain both S and H.

We constructed a diffraction intensity map for the new phase using the most intense line. The map shows that the phase is populated mostly near the rim of the laser-heated spot (Figure 5b). The chemical maps of the same heated spot also reveal a rim like structure around the hot spot. The areas can be divided into: (a) non-reacted material around the heated area of Fe_3S composition as confirmed by point analysis (the green area in the S map), (b) S-poor/free areas at the laser-heated center most likely the remnants of unquenchable FeH converted into Fe metal, and (c) S-rich areas at the rim of the heated spot (the red rim in the S map). As shown in the figure, the new phase is located in the S-rich area and therefore should contain higher S content than the starting material, Fe_3S. The S-rich rim area should also have FeS(VI) as well as the new phase according to our X-ray diffraction analysis. Unfortunately, our EPMA results cannot resolve the difference in Fe:S ratio between FeS(VI) and the new phase. The reason for this is that the typical grain size of the phases in LHDAC experiments is a few hundreds of nanometers. The thickness of the recovered sample is approximately 10 μm, and the excitation depths by the electron beam should be large enough for the thickness. Therefore, phases beneath the surface could contaminate the chemical composition measured in the EMPA of the LHDAC recovered sample. For accurate measurements, thinning of the heated area using focused ion beam (FIB) and chemical analysis in Transmission Electron Microscopy would be required. However, samples synthesized in a H medium are mechanically weak and were not suitable for such sample

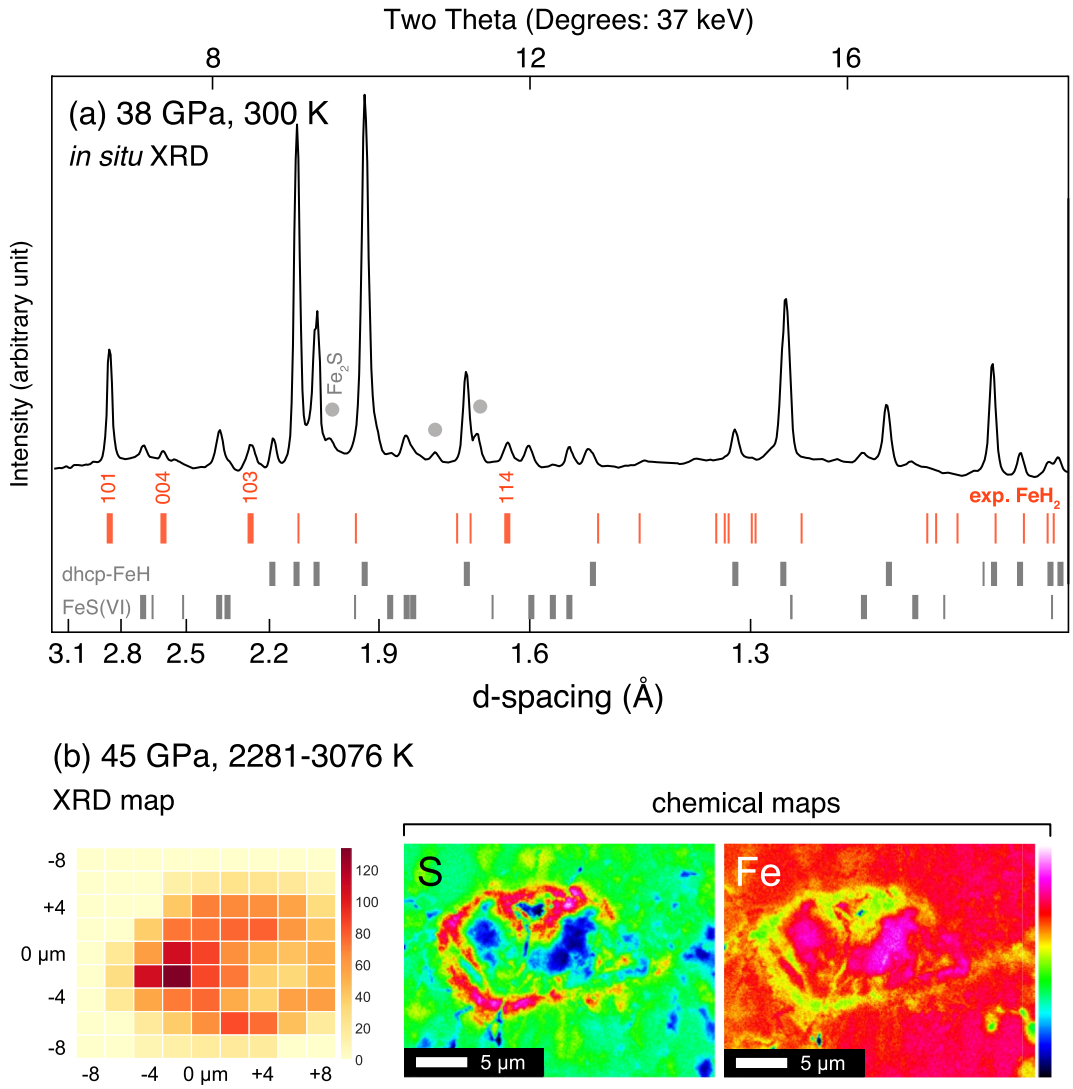

Figure 5. (a) An X-ray diffraction pattern for the new phase at 38 GPa and 300 K upon temperature quench after reaction of Fe_3S + H at temperatures in the 1700–4460 K range. The thin vertical ticks show all the expected *d*-spacing and intensity for a given phase and the thick vertical ticks highlight the observed ones. The expanded FeH_2 (red ticks) structure provides the best fit for the new observed peaks with four peaks uniquely matching without overlaps with other phases (bold ticks). Additionally, peaks at 2.1, 1.7, and 1.1 Å, while overlapping peaks from other phases, can also match and to some degree enhance the intensity of observed peaks. The gray dots indicate weak peaks, which can be assigned to a small amount of Fe_2S. (b) A map of the diffraction intensity of the FeS_xH_y 101 peak in the laser heated area from run r320 at 45 GPa (starting with Fe_3S + H_2) (left). The map was constructed from diffraction patterns collected after temperature quench in a 16 × 16 μm grid with 2 μm steps. The map shows that the phase is populated in the outer part of the heated area. Composition maps for S and Fe (right) of the recovered heated area show that the center of the heated spot is mostly Fe-rich while the edge is more S-rich. A backscattered electron image of the area is presented in Figure S2 in Supporting Information S1.

processing. Despite the limitation, EPMA strongly indicates that the molar ratio between Fe and S should be close to 1:1 rather than 3:1 of the starting material.

The temperature conditions for the sample shown in Figure 5b were sufficiently high for the melting of an Fe-S-H alloy. In fact, the compositional distribution found in the analysis resembles those reported for melting in previous LHDAC studies (e.g., Andrault et al., 2012). Those studies found melt at the center while liquidus phases at the outer rim. The same interpretation appears to be applicable for this sample, as the center is likely former FeH_x (from nearly pure Fe without much S), which may have a lower melting temperature; while the rim contains FeS and FeS_xH_y, which may have higher melting temperatures. There-

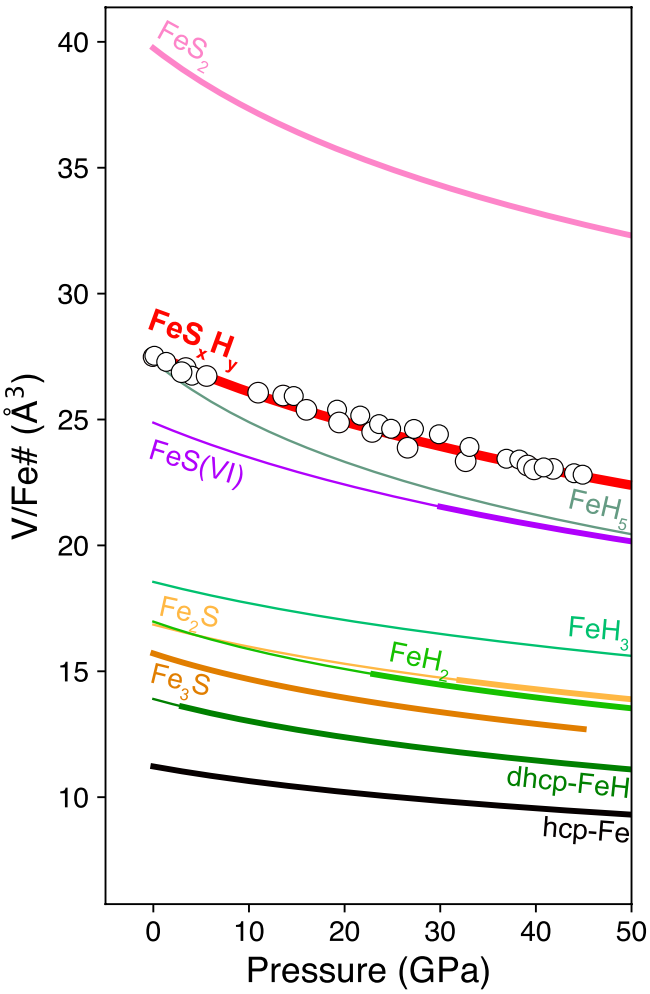

Figure 6. Pressure-volume relation of the new phase (FeS_xH_y, open circles) and the fitted equation of state (the thick red curve). We also show other phases in the Fe-S and Fe-H systems from the literature for comparison (thick lines correspond to the pressure range at which the phase is observed to be stable; thin lines correspond to pressure range outside the phase stability where the fitted volume is extrapolated). Fe: Dewaele et al. (2006); dhcp FeH, FeH_2 and FeH_3: Pépin et al. (2014); FeH_5: Pépin et al. (2017); Fe_3S: Kamada, Ohtani, Terasaki, et al. (2014); Fe_2S: Zurkowski (2020); FeS(VI): Ono and Kikegawa (2006); and FeS_2: Merkel et al. (2002). The unit-cell volumes are divided by the number of Fe atoms in the unit cell. Note that we assume the new phase has the same number of Fe atoms as regular FeH_2, which is 4. The data points are provided in Table S5 in Supporting Information S1.

fore, the distribution may be a consequence of crystallization of FeS and FeS_xH_y from a Fe-S-H liquid, which would then enrich the melt with H relative to S.

While the exact ratio between Fe and S is unknown for the new phase, as discussed, EPMA results combined with XRD analysis can constrain the ratio to be close to 1:1. We performed unit-cell volume measurement during decompression to 1 bar for the new phase synthesized in two runs (r220 and r231c; Figure 6). While the measured volume of the new phase is very close to that of FeS(VI), it is systematically greater throughout the pressure range. Increasing solubility of H in iron-hydrogen alloys at high pressure has shown to contribute to increase in unit-cell volumes (e.g., Badding et al., 1991; Narygina et al., 2011; Pépin et al., 2014). Fitting to a Vinet equation (Vinet et al., 1987) for fixed pressure derivative of bulk modulus ($K_0' = 4$) yielded $V_0 = 110.4(5)$ and $K_0 = 159(7)$ for the new phase. We note that the fitting was performed under an assumption that the chemical composition of the new phase remains constant at different synthesis pressures. However, it is possible that H content varies, which might have caused some data scatter. The equation of state curve of the new phase is nearly parallel to that of FeS(VI), and therefore, the volume difference between FeS(VI) and the new phase remains nearly constant within the pressure range.

Figure 6 shows the volume per one Fe of the phases in the Fe-H and Fe-S system. Such a representation gives qualitative insights on how substituting S and H would increase the volume of Fe alloys. However, this representation requires knowledge of the number of formula units in the unit-cell (Z). The Z number is unknown for the new FeS_xH_y phase. Since we indexed the diffraction lines of the new phase to a tetragonal FeH_2-like structure, we choose to use the same Z number (4). We calculated the volume differences between hcp-Fe and different iron sulfides and iron hydrides, as well as between iron hydrides and iron sulfides themselves (Table S6 in Supporting Information S1). We obtained an average value for $\Delta V(\mathrm{H}) = 2.02$ Å^3 corresponding to the average volume increase caused by one atom of H (Table S6 in Supporting Information S1). Therefore, the near constant volume difference between FeS(VI) and the new phase can be explained by $y \approx 1$ for FeS_xH_y where $x = 1$ from the EMPA data. While the assignment for the new phase here remains tentative because of the uncertainties in the crystal structure, from the arguments above built from our observations, it is reasonable to assume that the new phase is close to FeS_xH_y with $x \approx 1$ and $y \approx 1$.

In pure Fe, H escapes from the crystal structure during decompression (Okuchi, 1997). As H expands the unit-cell volume, H loss can result in a sudden volume decrease. For the new FeS_xH_y ($x \approx 1$ and $y \approx 1$) phase, we did not observe any significant volume decrease during decompression and the measured P-V data show a smooth trend extended close to 1 bar (Figure 6). At 1 bar, the diffraction patterns of the sample quenched from 42 GPa show some new diffraction peaks as well as those existing at high pressures and assigned to the new phase (Figure S4 in Supporting Information S1). The new lines appearing in the quench diffraction pattern could not be indexed with any known phases in Fe-S. It is feasible that FeS_xH_y ($x \approx 1$ and $y \approx 1$) may convert to a different crystal structure (either partially or completely) at 1 bar. Therefore, it is difficult to index the diffraction lines, and the volume of the new phase remains uncertain at 1 bar.

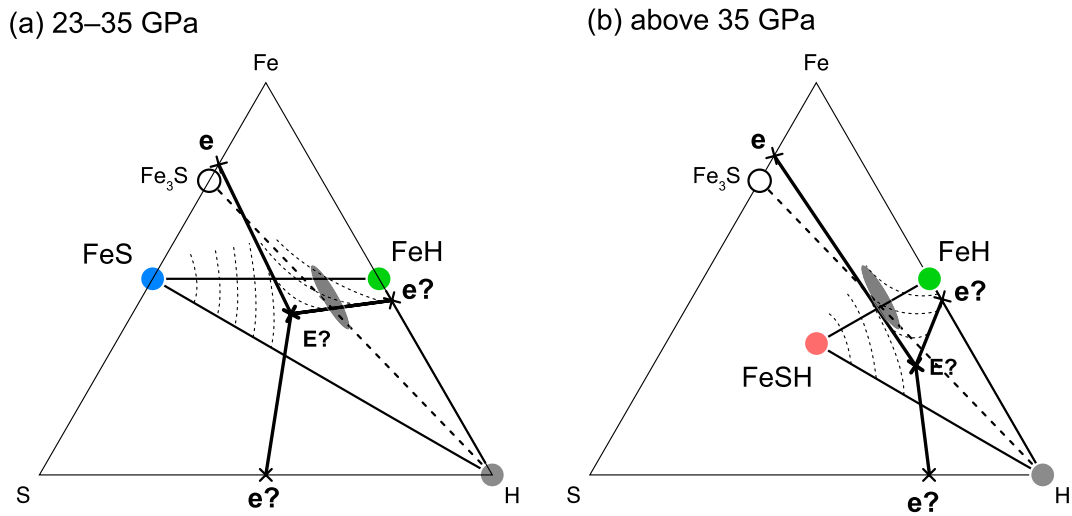

Figure 7. Provisional ternary Fe-S-H phase diagrams at 23–35 GPa (a) and above 35 GPa (b). *e*'s show the eutectic points in the Fe-S, Fe-H and H-S binaries and *E* is the eutectic of the ternary. The colored circles show major phases observed at the pressures. The thick dashed lines connect the starting phases. The thin dashed lines represent possible isotherms. We show the Fe:S:H ratios from the two models presented in Stähler et al. (2021) to explain a very large Martian core (therefore low density) recently found by the InSight seismic observation: Fe-5wt%O-16wt%S-1wt%H-1wt%C ($Fe_{0.42}O_{0.10}S_{0.15}H_{0.30}C_{0.03}$ in mole fraction) and Fe-5wt%O-16wt%S-2wt%H ($Fe_{0.33}O_{0.07}S_{0.12}H_{0.48}$ in mole fraction). For the plot in this diagram (the gray ovals), we renormalized the mole fraction for the ratios between Fe:S:H only, which increases content H by 4%. Note that the details of these diagrams remain uncertain and therefore the diagrams should be regarded as tentative.

4. Discussion

4.1. Phase Relations in Fe-S-H Up to 45 GPa

In all our experimental runs, we observed the striking disappearance of Fe_3S upon heating in a H-rich environment, regardless of pressure, temperature, and starting composition between Fe and FeS. The formation of FeH (dhcp or fcc) is also common to all the runs. The differences observed between runs are whether FeS or FeS_xH_y ($x \approx 1$ and $y \approx 1$) was the main S-bearing phase at high pressure and high temperature. Although we do not have tight constraints on the melting behaviors of the studied system, we observed some clear pressure-dependent changes in the Fe_3S + H experiments. Based on the information, we built provisional ternary Fe-S-H phase diagrams in Figure 7.

At 23–35 GPa, we observed FeH and FeS phases in temperature quench (Figure 7a). However, according to Gibbs' phase rule, if a thermodynamical equilibrium is reached (possibly locally in LHDAC), three phases are expected for a degree of freedom of 2. Although the third phase remains uncertain, it should not contain Fe, otherwise it would appear in XRD patterns. Therefore, we tentatively assign the third phase to H. It is feasible that a H-S phase instead is stable in our experimental runs. The Fe-S binary phase diagram is well constrained at pressures in the 23–40 GPa range (Stewart et al., 2007) and features a eutectic behavior with eutectic composition close to Fe_3S at pressures below 35 GPa. The Fe-H binary phase diagram, on the other hand, is less well constrained but likely features a solid-solution for FeH_x where $x \leq 1$. Shibazaki et al. (2014) proposed an Fe-H binary phase diagram featuring a eutectic for $x > 1$ in FeH_x at 15 GPa. However, the subsequent discovery of FeH_2, FeH_3 (Pépin et al., 2014), and FeH_5 (Pépin et al., 2017) at higher pressures raises questions on the position of the eutectic along the Fe-H join. Although many aspects of the phase diagram shown in Figure 7a remain tentative, the crystallization of the FeS and FeH phases in our study at the pressure range is at least consistent with a global ternary eutectic point in the phase diagram.

Above 35 GPa after extended cycles of heating runs, only FeH and FeS_xH_y ($x \approx 1$ and $y \approx 1$) remained from the reaction of Fe_3S with H_2, whereas FeS almost completely disappears (Figure 7b). As discussed above, from the texture in Figure 5, it is feasible that FeS_xH_y is the first solid phase that crystallizes from an Fe-S-H liquid. Similar to the case at 23–35 GPa, we assume that either H or H-S phase exists as the third phase. The

key observation at this pressure range is that FeS is unlikely to be stable anymore and a phase including both S and H may appear in the phase diagram. Assuming that eutectic behavior along all three joins persists with increasing pressure, the position of the ternary eutectic may move toward the H end-member. However, the precise positions of the eutectic points remain to be constrained through additional experiments.

4.2. Implications for Crystallization of Mars-Sized Planetary Cores

The pressure range we studied for Fe-S-H overlaps with the range expected for the Martian core, 20–40 GPa (Helffrich, 2017). For the Martian core, sulfur has been considered as the main light element based on its abundance in Martian meteorites and theoretical models of nebular condensation (Dreibus & Wänke, 1985; Lodders & Fegley, 1997; Wänke & Dreibus, 1988). Although there are different views (Wang & Becker, 2017), existing models prefer 14%–17% of S in the Martian core (Gaetani & Grove, 1997; Khan et al., 2017; Urakawa et al., 2004), which is close to Fe_3S. The amount of hydrogen stored in the Martian core is currently unknown. For the Martian mantle, recent estimates (100–300 wt ppm in H_2O) are at least similar to that of the Earth's mantle (Hallis et al., 2012; Leshin, 2000; McCubbin et al., 2010; Usui et al., 2012). Therefore, H remains as a viable candidate for a light element in the Martian core, as it can partition preferentially to the core from its affinity to metal at high pressures (Tagawa et al., 2021).

Recent data analysis of seismic data from the InSight mission showed that the Martian core is much larger than previously thought and therefore require much smaller density for the given mass and much larger amounts of light elements (Stähler et al., 2021). The study found that S content has to exceed the cosmochemically estimated value in order to explain the large density deficit only by S. This observation may suggest significant presence of other light elements in the Martian core. Although the exact kinds and amounts of light elements remain uncertain, they found that a few hydrogen-containing models can explain the observations, such as Fe-5wt%O-16wt%S-1wt%H-1wt%C ($Fe_{0.42}O_{0.10}S_{0.15}H_{0.30}C_{0.03}$ in mole fraction) and Fe-5wt%O-16wt%S-2wt%H ($Fe_{0.33}O_{0.07}S_{0.12}H_{0.48}$ in mole fraction). As shown in Figure 7, these H-bearing models overlap with the ternary triangles we constructed based on our observation, suggesting the relevance of our observations to the models. Therefore, the crystallization of alloys in Fe-S-H from iron-rich liquid studied here could contribute to the understanding of the Martian core. Our experimental study also provides essential data to model the cores of Mars-sized planets found outside of the solar system (Jontof-Hutter et al., 2015). While detection and mass measurement are very challenging because of their small size, with their potential habitability and improved technology in coming missions, more data will likely be available for Mars-sized exoplanets.

According to our experimental observations, at 23–35 GPa (therefore, at much of the Martian core or at the core of sub-Mars), either FeS or FeH_x would crystallize first depending on the S/H ratio of the system, if the core contains more than 1 wt% H. For example, if the bulk composition of the system is on the S-rich side (left of the eutectic line in Figure 7a), FeS would likely be the first solid to crystallize and the liquid would become progressively enriched in H as crystallization of FeS proceeds. Layering of the core would then depend on the density contrast between the different phases, as well as mixing properties and local dynamics at play. The density difference between liquid FeH_x and liquid FeS is not known. However, solid FeH_x is denser than solid FeS because H tends to be incorporated in the interstitial site of the densely packed structure of Fe. If such a relationship is applicable between solid FeS and liquid FeH_x, solid FeS could even "float" at the outer part of the core. Above 35 GPa (therefore, at the innermost Martian core or at the cores of super-Mars and sub-Earths), the appearance of a new FeS_xH_y ($x \approx 1$ and $y \approx 1$) phase could change the crystallization of the core. In this case, either FeS_xH_y ($x \approx 1$ and $y \approx 1$) or FeH_x would crystallize first while our observation in Figure 5 appears to support the former. H would likely decrease the melting temperature of the new phase below that of Fe-S, but whether it would decrease the melting temperature below that of Fe-H is unknown. A few important measurements are therefore to be made to further understand Fe-S-H ternary in Mars-sized rocky planets' cores. Measurements of melting of FeS_xH_y ($x \approx 1$ and $y \approx 1$) are needed to further constrain the crystallization behavior of the system above 35 GPa. Our data mostly reside on the H rich side of the Fe-S-H ternary (Figure 7). Although some of the phases we identified here could still appear in low H systems, it would be important to conduct measurements on systems with smaller amounts of H, which would be more relevant for planets with a smaller amount of H (< 1 wt%).

Although not directly relevant to the Earth, our results shed additional light on the complexity of light element partitioning between solid and liquid Fe, especially when H is involved. The observed density difference between the solid and liquid Earth's core suggests that the liquid outer core is enriched in light elements with respect to the solid inner core (Birch, 1952; Poirier, 1994). Melting experiments on Fe-S alloys have shown that all light elements do not necessarily preferentially partition into liquid Fe. Mori et al. (2017) showed that the partition coefficient of S between solid and liquid iron increases with increasing pressure and the trend persists up to 254 GPa, which in turn suggests that with increasing pressure S tends to be more soluble into solid Fe than into liquid Fe. The preferential partitioning of S toward solid Fe with increasing pressure was later confirmed by Yokoo et al. (2019) who performed melting experiments on the Fe-O-S system up to 208 GPa. Our study of the Fe-S-H system at 23–35 GPa confirms what has been observed in the literature for Fe-C-H (Hirose et al., 2019; Narygina et al., 2011; Ohta et al., 2019) and Fe-O-H up to 80 GPa (Liu et al., 2017; Ohtani et al., 2005; Yuan et al., 2018): H may not necessarily alloy with other light elements but could preferentially partition into a phase that does not contain the other light element. However, like in the Fe-O-H system above 80 GPa with the formation of FeOOH, pressure appears to promote the formation of a ternary alloy (FeS_xH_y, where $x \approx 1$ and $y \approx 1$; the new phase we observed) in Fe-S-H as well, albeit at a lower pressure. The relevance of FeS_xH_y ($x \approx 1$ and $y \approx 1$) for Earth-size planets remains to be tested at the required pressures, temperature, and compositional conditions. If this behavior was to persist up to Earth's core pressure, and given that S prefers solid Fe, upon crystallization of a Fe-S-H rich core, an inner core could be enriched in S, whereas the liquid outer core could be enriched in H.

First principle studies have shown that H can explain the density and compressional velocity of the Earth's outer core and therefore could be the primary light element in the outer core up to 1 wt.% (Umemoto & Hirose, 2015). However, Caracas (2015) showed that solid Fe-H cannot explain the shear velocities observed in the inner outer core. Therefore, another light element like S or a combination of light elements with an affinity for solid iron could be the primary light element(s) in the inner core.

Conflict of Interest

The authors declare no conflicts of interest relevant to this study.

Acknowledgments
We thank the editor and two anonymous reviewers for helpful comments to improve this paper. This work has been supported by grants NSF-AST2005567 and NASA-80NSSC18K0353. H. Piet and S.-H. Shim were supported partially by the Keck Foundation. The results reported herein benefit from collaborations and information exchange within NASA's Nexus for Exoplanet System Science (NExSS) research coordination network sponsored by NASA's Science Mission Directorate. Synchrotron experiments were conducted at GeoSoilEnviroCARS (University of Chicago, Sector 13), Advanced Photon Source (APS). GeoSoilEnviroCARS is supported by the NSF-Earth Science (EAR-1634415) and DOE-GeoScience (DE-FG02-94ER14466). APS is supported by DOE-BES under contract DE-AC02-06CH11357. We acknowledge the use of facilities within the Eyring Materials Center at Arizona State University supported in part by NNCI-ECCS-1542160. We would also like to acknowledge Axel Wittmann from the Eyring Materials Center at Arizona State University supported in part by NNCI-ECCS-1542160 for his assistance with EPMA measurements.

Data Availability Statement

Data sets for this research are included in this paper (and its Supporting Information S1 files) (Piet et al., 2021).

References

Andrault, D., Petitgirard, S., Nigro, G. L., Devidal, J.-L., Veronesi, G., Garbarino, G., & Mezouar, M. (2012). Solid–liquid iron partitioning in Earth's deep mantle. *Nature*, *487*(7407), 354–357. https://doi.org/10.1038/nature11294

Anzellini, S., Dewaele, A., Mezouar, M., Loubeyre, P., & Morard, G. (2013). Melting of iron at Earth's inner core boundary based on fast X-ray diffraction. *Science*, *340*(6131), 464–466. https://doi.org/10.1126/science.1233514

Badding, J. V., Hemley, R., & Mao, H. (1991). High-pressure chemistry of hydrogen in metals: In situ study of iron hydride. *Science*, *253*(5018), 421–424. https://doi.org/10.1126/science.253.5018.421

Badro, J., Côté, A. S., & Brodholt, J. P. (2014). A seismologically consistent compositional model of Earth's core. *Proceedings of the National Academy of Sciences*, *111*(21), 7542–7545. https://doi.org/10.1073/pnas.1316708111

Birch, F. (1952). Elasticity and constitution of the Earth's interior. *Journal of Geophysical Research*, *57*(2), 227–286. https://doi.org/10.1029/jz057i002p00227

Boehler, R. (1992). Melting of the Fe-FeO and the Fe-FeS systems at high pressure: Constraints on core temperatures. *Earth and Planetary Science Letters*, *111*(2–4), 217–227. https://doi.org/10.1016/0012-821x(92)90180-4

Caracas, R. (2015). The influence of hydrogen on the seismic properties of solid iron. *Geophysical Research Letters*, *42*(10), 3780–3785. https://doi.org/10.1002/2015gl063478

Deemyad, S., & Silvera, I. F. (2008). Melting line of hydrogen at high pressures. *Physical Review Letters*, *100*(15), 155701. https://doi.org/10.1103/physrevlett.100.155701

Deemyad, S., Sterer, E., Barthel, C., Rekhi, S., Tempere, J., & Silvera, I. F. (2005). Pulsed laser heating and temperature determination in a diamond anvil cell. *Review of Scientific Instruments*, *76*(12), 125104. https://doi.org/10.1063/1.2140493

Dewaele, A., Fiquet, G., & Gillet, P. (1998). Temperature and pressure distribution in the laser-heated diamond–anvil cell. *Review of Scientific Instruments*, *69*(6), 2421–2426. https://doi.org/10.1063/1.1148970

Dewaele, A., Loubeyre, P., Occelli, F., Mezouar, M., Dorogokupets, P. I., & Torrent, M. (2006). Quasihydrostatic equation of state of iron above 2 Mbar. *Physical Review Letters*, *97*(21), 215504. https://doi.org/10.1103/physrevlett.97.215504

Dreibus, G., & Wänke, H. (1985). Mars, a volatile-rich planet. *Meteoritics*, *20*, 367–381.

Duan, D., Liu, Y., Tian, F., Li, D., Huang, X., Zhao, Z., et al. (2014). Pressure-induced metallization of dense $(H_2S)_2H_2$ with high-Tc superconductivity. *Scientific Reports*, *4*, 6968. https://doi.org/10.1038/srep06968

Fei, Y., Li, J., Bertka, C. M., & Prewitt, C. T. (2000). Structure type and bulk modulus of Fe_3S, a new iron-sulfur compound. *American Mineralogist*, *85*(11–12), 1830–1833. https://doi.org/10.2138/am-2000-11-1229

Fei, Y., Prewitt, C. T., Mao, H.-K., & Bertka, C. M. (1995). Structure and density of FeS at high pressure and high temperature and the internal structure of Mars. *Science*, *268*(5219), 1892–1894. https://doi.org/10.1126/science.268.5219.1892

Gaetani, G. A., & Grove, T. L. (1997). Partitioning of moderately siderophile elements among olivine, silicate melt, and sulfide melt: Constraints on core formation in the Earth and Mars. *Geochimica et Cosmochimica Acta*, *61*, 1829–1846. https://doi.org/10.1016/s0016-7037(97)00033-1

Goncharov, A. F., Prakapenka, V. B., Struzhkin, V. V., Kantor, I., Rivers, M. L., & Dalton, D. A. (2010). X-ray diffraction in the pulsed laser heated diamond anvil cell. *Review of Scientific Instruments*, *81*(11), 113902. https://doi.org/10.1063/1.3499358

Hallis, L. J., Taylor, G. J., Nagashima, K., & Huss, G. R. (2012). Magmatic water in the martian meteorite Nakhla. *Earth and Planetary Science Letters*, *359*, 84–92. https://doi.org/10.1016/j.epsl.2012.09.049

Helffrich, G. (2017). Mars core structure—Concise review and anticipated insights from InSight. *Progress in Earth and Planetary Science*, *4*(1), 1–14. https://doi.org/10.1186/s40645-017-0139-4

Hirose, K., Tagawa, S., Kuwayama, Y., Sinmyo, R., Morard, G., Ohishi, Y., & Genda, H. (2019). Hydrogen limits carbon in liquid iron. *Geophysical Research Letters*, *46*(10), 5190–5197. https://doi.org/10.1029/2019gl082591

Jontof-Hutter, D., Rowe, J. F., Lissauer, J. J., Fabrycky, D. C., & Ford, E. B. (2015). The mass of the Mars-sized exoplanet Kepler-138b from transit timing. *Nature*, *522*(7556), 321–323. https://doi.org/10.1038/nature14494

Kamada, S., Ohtani, E., Fukui, H., Sakai, T., Terasaki, H., Takahashi, S., et al. (2014). The sound velocity measurements of Fe_3S. *American Mineralogist*, *99*(1), 98–251. https://doi.org/10.2138/am.2014.4463

Kamada, S., Ohtani, E., Terasaki, H., Sakai, T., Takahashi, S., Hirao, N., & Ohishi, Y. (2014). Equation of state of Fe_3S at room temperature up to 2 megabars. *Physics of the Earth and Planetary Interiors*, *228*, 106–113. https://doi.org/10.1016/j.pepi.2013.11.001

Kamada, S., Terasaki, H., Ohtani, E., Sakai, T., Kikegawa, T., Ohishi, Y., et al. (2010). Phase relationships of the Fe–FeS system in conditions up to the Earth's outer core. *Earth and Planetary Science Letters*, *294*(1–2), 94–100. https://doi.org/10.1016/j.epsl.2010.03.011

Kato, C., Umemoto, K., Ohta, K., Tagawa, S., Hirose, K., & Ohishi, Y. (2020). Stability of fcc phase FeH to 137 GPa. *American Mineralogist: Journal of Earth and Planetary Materials*, *105*(6), 917–921. https://doi.org/10.2138/am-2020-7153

Kavner, A., Duffy, T. S., & Shen, G. (2001). Phase stability and density of FeS at high pressures and temperatures: Implications for the interior structure of Mars. *Earth and Planetary Science Letters*, *185*(1–2), 25–33. https://doi.org/10.1016/s0012-821x(00)00356-3

Khan, A., Liebske, C., Rozel, A., Rivoldini, A., Nimmo, F., Connoly, J. A. D., et al. (2017). *A geophysical perspective on the bulk composition of Mars*. https://doi.org/10.1002/2017JE005371

Kusaba, K., Syono, Y., Kikegawa, T., & Shimomura, O. (1997). Structure of FeS under high pressure. *Journal of Physics and Chemistry of Solids*, *58*(2), 241–246. https://doi.org/10.1016/s0022-3697(96)00120-5

Leinenweber, K. D., Tyburczy, J. A., Sharp, T. G., Soignard, E., Diedrich, T., Petuskey, W. B., et al. (2012). Cell assemblies for reproducible multi-anvil experiments (the COMPRES assemblies). *American Mineralogist*, *97*(2–3), 353–368. https://doi.org/10.2138/am.2012.3844

Leshin, L. A. (2000). Insights into martian water reservoirs from analyses of martian meteorite QUE94201. *Geophysical Research Letters*, *27*, 2017–2020. https://doi.org/10.1029/1999gl008455

Li, J., & Agee, C. (2001). Element partitioning constraints on the light element composition of the Earth's core. *Geophysical Research Letters*, *28*(1), 81–84. https://doi.org/10.1029/2000gl012114

Liu, J., Hu, Q., Kim, D. Y., Wu, Z., Wang, W., Xiao, Y., et al. (2017). Hydrogen-bearing iron peroxide and the origin of ultralow-velocity zones. *Nature*, *551*(7681), 494–497. https://doi.org/10.1038/nature24461

Lodders, K., & Fegley, B. (1997). An oxygen isotope model for the composition of Mars. *Icarus*, *126*, 373–394. https://doi.org/10.1006/icar.1996.5653

Mao, H., Xu, J.-A., & Bell, P. (1986). Calibration of the ruby pressure gauge to 800 kbar under quasi-hydrostatic conditions. *Journal of Geophysical Research: Solid Earth*, *91*(B5), 4673–4676. https://doi.org/10.1029/jb091ib05p04673

McCubbin, F. M., Smirnov, A., Nekvasil, H., Wang, J., Hauri, E., & Lindsley, D. H. (2010). Hydrous magmatism on Mars: A source of water for the surface and subsurface during the Amazonian. *Earth and Planetary Science Letters*, *292*, 132–138. https://doi.org/10.1016/j.epsl.2010.01.028

Merkel, S., Jephcoat, A., Shu, J., Mao, H.-K., Gillet, P., & Hemley, R. (2002). Equation of state, elasticity, and shear strength of pyrite under high pressure. *Physics and Chemistry of Minerals*, *29*(1), 1–9. https://doi.org/10.1007/s002690100207

Morard, G., Sanloup, C., Fiquet, G., Mezouar, M., Rey, N., Poloni, R., & Beck, P. (2007). Structure of eutectic Fe–FeS melts to pressures up to 17 GPa: Implications for planetary cores. *Earth and Planetary Science Letters*, *263*(1–2), 128–139. https://doi.org/10.1016/j.epsl.2007.09.009

Mori, Y., Ozawa, H., Hirose, K., Sinmyo, R., Tateno, S., Morard, G., & Ohishi, Y. (2017). Melting experiments on Fe–Fe_3S system to 254 GPa. *Earth and Planetary Science Letters*, *464*, 135–141. https://doi.org/10.1016/j.epsl.2017.02.021

Narygina, O., Dubrovinsky, L. S., McCammon, C. A., Kurnosov, A., Kantor, I. Y., Prakapenka, V. B., & Dubrovinskaia, N. A. (2011). X-ray diffraction and Mössbauer spectroscopy study of fcc iron hydride FeH at high pressures and implications for the composition of the Earth's core. *Earth and Planetary Science Letters*, *307*(3–4), 409–414. https://doi.org/10.1016/j.epsl.2011.05.015

Nishida, K., Shibazaki, Y., Terasaki, H., Higo, Y., Suzuki, A., Funamori, N., & Hirose, K. (2020). Effect of sulfur on sound velocity of liquid iron under martian core conditions. *Nature Communications*, *11*(1), 1–5. https://doi.org/10.1038/s41467-020-15755-2

Ohfuji, H., Sata, N., Kobayashi, H., Ohishi, Y., Hirose, K., & Irifune, T. (2007). A new high-pressure and high-temperature polymorph of FeS. *Physics and Chemistry of Minerals*, *34*(5), 335–343. https://doi.org/10.1007/s00269-007-0151-0

Ohta, K., Suehiro, S., Hirose, K., & Ohishi, Y. (2019). Electrical resistivity of fcc phase iron hydrides at high pressures and temperatures. *Comptes Rendus Geoscience*, *351*(2–3), 147–153. https://doi.org/10.1016/j.crte.2018.05.004

Ohtani, E., Hirao, N., Kondo, T., Ito, M., & Kikegawa, T. (2005). Iron-water reaction at high pressure and temperature, and hydrogen transport into the core. *Physics and Chemistry of Minerals*, *32*(1), 77–82. https://doi.org/10.1007/s00269-004-0443-6

Okuchi, T. (1997). Hydrogen partitioning into molten iron at high pressure: Implications for Earth's core. *Science*, *278*(5344), 1781–1784. https://doi.org/10.1126/science.278.5344.1781

Ono, S., & Kikegawa, T. (2006). High-pressure study of FeS, between 20 and 120 GPa, using synchrotron X-ray powder diffraction. *American Mineralogist*, *91*(11–12), 1941–1944. https://doi.org/10.2138/am.2006.2347

Ozawa, H., Hirose, K., Suzuki, T., Ohishi, Y., & Hirao, N. (2013). Decomposition of Fe_3S above 250 GPa. *Geophysical Research Letters*, *40*(18), 4845–4849. https://doi.org/10.1002/grl.50946

Pépin, C. M., Dewaele, A., Geneste, G., Loubeyre, P., & Mezouar, M. (2014). New iron hydrides under high pressure. *Physical Review Letters*, *113*(26), 265504. https://doi.org/10.1103/physrevlett.113.265504

Pépin, C. M., Geneste, G., Dewaele, A., Mezouar, M., & Loubeyre, P. (2017). Synthesis of FeH_5: A layered structure with atomic hydrogen slabs. *Science*, *357*(6349), 382–385. https://doi.org/10.1126/science.aan0961

Piet, H., Leinenweber, K., Greenberg, E., Prakapenka, V. B., & Shim, S.-H. (2021). *Effects of hydrogen on the phase relations in Fe–FeS at pressures of Mars-sized bodies—Datasets*. Zenodo. https://doi.org/10.5281/zenodo.4738360

Poirier, J.-P. (1994). Light elements in the earth's outer core: A critical review. *Physics of the Earth and Planetary Interiors*, *85*(3–4), 319–337. https://doi.org/10.1016/0031-9201(94)90120-1

Prakapenka, V., Kubo, A., Kuznetsov, A., Laskin, A., Shkurikhin, O., Dera, P., et al. (2008). Advanced flat top laser heating system for high pressure research at GSECARS: Application to the melting behavior of germanium. *High Pressure Research*, *28*(3), 225–235. https://doi.org/10.1080/08957950802050718

Prescher, C., & Prakapenka, V. B. (2015). DIOPTAS: A program for reduction of two-dimensional X-ray diffraction data and data exploration. *High Pressure Research*, *35*(3), 223–230. https://doi.org/10.1080/08957959.2015.1059835

Sakamaki, K., Takahashi, E., Nakajima, Y., Nishihara, Y., Funakoshi, K., Suzuki, T., & Fukai, Y. (2009). Melting phase relation of FeH_x up to 20 GPa: Implication for the temperature of the Earth's core. *Physics of the Earth and Planetary Interiors*, *174*(1–4), 192–201. https://doi.org/10.1016/j.pepi.2008.05.017

Shibazaki, Y., Ohtani, E., Terasaki, H., Tateyama, R., Sakamaki, T., Tsuchiya, T., & Funakoshi, K.-I. (2011). Effect of hydrogen on the melting temperature of FeS at high pressure: Implications for the core of Ganymede. *Earth and Planetary Science Letters*, *301*(1–2), 153–158. https://doi.org/10.1016/j.epsl.2010.10.033

Shibazaki, Y., Terasaki, H., Ohtani, E., Tateyama, R., Nishida, K., Funakoshi, K.-I., & Higo, Y. (2014). High-pressure and high-temperature phase diagram for Fe0.9Ni0.1–H alloy. *Physics of the Earth and Planetary Interiors*, *228*, 192–201. https://doi.org/10.1016/j.pepi.2013.12.013

Shim, S.-H. (2017). *PeakPo—A python software for X-ray diffraction analysis at high pressure and high temperature*. https://doi.org/10.5281/zenodo.1193836

Stähler, S. C., Khan, A., Banerdt, W. B., Lognonné, P., Giardini, D., Ceylan, S., et al. (2021). Seismic detection of the martian core. *Science*, *373*(6553), 443–448. https://doi.org/10.1126/science.abi7730

Stewart, A. J., Schmidt, M. W., Van Westrenen, W., & Liebske, C. (2007). Mars: A new core-crystallization regime. *Science*, *316*(5829), 1323–1325. https://doi.org/10.1126/science.1140549

Strobel, T. A., Ganesh, P., Somayazulu, M., Kent, P. R. C., & Hemley, R. J. (2011). Novel cooperative interactions and structural ordering in H_2S-H_2. *Physical Review Letters*, *107*(25), 255503. https://doi.org/10.1103/physrevlett.107.255503

Tagawa, S., Ohta, K., Hirose, K., Kato, C., & Ohishi, Y. (2016). Compression of Fe–Si–H alloys to core pressures. *Geophysical Research Letters*, *43*(8), 3686–3692. https://doi.org/10.1002/2016gl068848

Tagawa, S., Sakamoto, N., Hirose, K., Yokoo, S., Hernlund, J., Ohishi, Y., & Yurimoto, H. (2021). Experimental evidence for hydrogen incorporation into Earth's core. *Nature Communications*, *12*(1), 1–8. https://doi.org/10.1038/s41467-021-22035-0

Thompson, E., Davis, A., Bi, W., Zhao, J., Alp, E., Zhang, D., et al. (2018). High-pressure geophysical properties of fcc phase FeH_x. *Geochemistry, Geophysics, Geosystems*, *19*(1), 305–314. https://doi.org/10.1002/2017gc007168

Umemoto, K., & Hirose, K. (2015). Liquid iron-hydrogen alloys at outer core conditions by first-principles calculations. *Geophysical Research Letters*, *42*(18), 7513–7520. https://doi.org/10.1002/2015gl065899

Urakawa, S., Someya, K., Terasaki, H., Katsura, T., Yokoshi, S., Funakoshi, K.-I., et al. (2004). Phase relationships and equations of state for FeS at high pressures and temperatures and implications for the internal structure of Mars. *Physics of the Earth and Planetary Interiors*, *143*, 469–479. https://doi.org/10.1016/j.pepi.2003.12.015

Usui, T., Alexander, C. M., Wang, J., Simon, J. I., & Jones, J. H. (2012). Origin of water and mantle–crust interactions on Mars inferred from hydrogen isotopes and volatile element abundances of olivine-hosted melt inclusions of primitive shergottites. *Earth and Planetary Science Letters*, *357*, 119–129. https://doi.org/10.1016/j.epsl.2012.09.008

Vinet, P., Ferrante, J., Rose, J. H., & Smith, J. R. (1987). Compressibility of solids. *Journal of Geophysical Research: Solid Earth*, *92*(B9), 9319–9325. https://doi.org/10.1029/jb092ib09p09319

Wade, J., & Wood, B. (2005). Core formation and the oxidation state of the Earth. *Earth and Planetary Science Letters*, *236*(1–2), 78–95. https://doi.org/10.1016/j.epsl.2005.05.017

Wang, Z., & Becker, H. (2017). Chalcophile elements in Martian meteorites indicate low sulfur content in the Martian interior and a volatile element-depleted late veneer. *Earth and Planetary Science Letters*, *463*, 56–68. https://doi.org/10.1016/j.epsl.2017.01.023

Wänke, H., & Dreibus, G. (1988). Chemical composition and accretion history of terrestrial planets. *Philosophical Transactions of the Royal Society of London - Series A: Mathematical and Physical Sciences*, *325*(1587), 545–557.

Ye, Y., Prakapenka, V., Meng, Y., & Shim, S.-H. (2017). Intercomparison of the gold, platinum, and MgO pressure scales up to 140 GPa and 2500 K. *Journal of Geophysical Research: Solid Earth*, *122*(5), 3450–3464. https://doi.org/10.1002/2016jb013811

Yokoo, S., Hirose, K., Sinmyo, R., & Tagawa, S. (2019). Melting experiments on liquidus phase relations in the Fe-S-O ternary system under core pressures. *Geophysical Research Letters*, *46*(10), 5137–5145. https://doi.org/10.1029/2019gl082277

Yuan, L., Ohtani, E., Ikuta, D., Kamada, S., Tsuchiya, J., Naohisa, H., et al. (2018). Chemical reactions between Fe and H_2O up to megabar pressures and implications for water storage in the Earth's mantle and core. *Geophysical Research Letters*, *45*(3), 1330–1338. https://doi.org/10.1002/2017gl075720

Zhang, G., Yukawa, H., Watanabe, N., Saito, Y., Fukaya, H., Morinaga, M., et al. (2008). Analysis of hydrogen diffusion coefficient during hydrogen permeation through pure niobium. *International Journal of Hydrogen Energy*, *33*(16), 4419–4423. https://doi.org/10.1016/j.ijhydene.2008.05.062

Zurkowski, C. (2020). *Stability of Fe2S and phase relations in the Fe–S–O system to 170 GPa and high temperatures* (Tech. Rep.). Knowledge@ UChicago.

Supporting Information for "Effects of Hydrogen on the Phase Relations in Fe–FeS at Pressures of Mars-Sized Bodies"

H. Piet[1], K. Leinenweber[2], E. Greenberg[3], V. B. Prakapenka[3], and S.-H. Shim[1]

[1]School of Earth and Space Exploration, Arizona State University, Tempe, Arizona 85287, U.S.A.

[2]School of Molecular Sciences, Arizona State University, Tempe, Arizona 85287, U.S.A.

[3]GeoSoilEnviroCars, University of Chicago, Chicago, Illinois 60439, U.S.A.

Contents of this file

1. Challenges in recovering sanmples synthesized in a H medium in laser-heated diamond-anvil cell

There are many complications in using extremely compressible hydrogen as a medium regarding the sample recovery from LHDAC experiments. Success rate for the recovery of the sample to 1 bar was low when we use H as a medium compared with other media. The main reasons are: (1) the diamond anvils fail much more frequently during heating even with pulsed laser heating; and (2) the sample chamber collapses frequently during decompression. The sample chamber collapse is particularly a severe problem, because the sample can be crushed by the collapse, and override the gasket (in this case, it is difficult to take out the sample foil from a Re gasket without chemical contamination). More frequent sample chamber collapse with a H medium is likely because of dynamic processes happening in the sample chamber during decompression: conversion of solid hydrogen to liquid hydrogen and then to H_2 gas. Fig. S2 shows a case where the sample chamber is completely collapsed and crushed.

For rare cases, we could find foils preserved after decompression. However, they are weak because of a lot of cracks as shown in Fig. S3. The cracking of the sample foil is likely because of vigorous flow of hydrogen medium when it converts from solid to liquid and then gas. We have only a smaller number of the samples recovered to 1 bar. For those cases, foil lifting often results in crumbling of the foil. Therefore, although we were

fully aware of the limitation of EPMA, we had to choose EPMA to obtain at least some level of chemical information on the samples.

2. Estimation for the Fe:S:H ratio of the experiments

For understanding the chemical reactions found in this study and relate those to the Fe-S-H phase diagram, it is important to know the ratio between hydrogen and the sample in our experiments. Because only a small part of the sample and H medium was reacted during laser heating which is a local heating, the ratio of interest in this case is determined by the amount of H and the sample inside the heated spot. Also, laser heating involves thermal gradients both axially and laterally (Fig. S6). Therefore, the ratio inside the volume at sufficient high temperature should be considered. It is also important to note that X-ray diffraction patterns were measured for a volume much smaller (approximately 30 μm^3) than the volume at high temperature (approximately 1500 μm^3).

We made a foil of iron sulfide by cold compressing the powder. Therefore, such a foil would have grain boundaries and micro-cracks (Figs S3 and S6). Hydrogen gas loading was performed at 1500 bar and therefore hydrogen should have infiltrated into the foil through the micro-cracks and grain boundaries (Fig. S3). Therefore, individual grain should have been surrounded by hydrogen. In this case, the H_2:Fe_3S molar ratio within the heated spot is determined by the porosity of the sample foil. Considering the molar volumes of H_2 and Fe_3S at 30 GPa (Loubeyre et al., 1996; Fei et al., 2000), we found that the molar ratio between H_2 and Fe_3S is approximately 1:2 within the laser heated spot, assuming 5% porosity. The molar ratio corresponds to 0.3 wt% H.

Some hydrogen outside of the heated volume of the sample foil could react at the sample/H_2 interface. If we assume that 1 μm thick H layers above and below the sample

foil as well as H in the pores were reacted with the sample, it would increase to 2.5 wt% H. Some amount of hydrogen may also circulate into the sample during heating while hydrogen at the grain boundaries are consumed, which would increase the amount of H for the sample. However, very short duration of heating, which would prevent the mobilization of a large amount of H, may reduce the effect of H from outside of the sample foil. The estimation we presented here involves many assumptions. Therefore, it will be important to improve our understanding on the sample environment in a H medium in LHDAC through numerical modelings or experiments in future studies.

References

Fei, Y., Li, J., Bertka, C. M., & Prewitt, C. T. (2000). Structure type and bulk modulus of Fe_3S, a new iron-sulfur compound. *American Mineralogist*, *85*(11-12), 1830–1833.

Kusaba, K., Syono, Y., Kikegawa, T., & Shimomura, O. (1997). Structure of FeS under high pressure. *Journal of Physics and Chemistry of Solids*, *58*(2), 241–246.

Loubeyre, P., LeToullec, R., Hausermann, D., Hanfland, M., Hemley, R., Mao, H., & Finger, L. (1996). X-ray diffraction and equation of state of hydrogen at megabar pressures. *Nature*, *383*(6602), 702–704.

Narygina, O., Dubrovinsky, L. S., McCammon, C. A., Kurnosov, A., Kantor, I. Y., Prakapenka, V. B., & Dubrovinskaia, N. A. (2011). X-ray diffraction and Mössbauer spectroscopy study of fcc iron hydride FeH at high pressures and implications for the composition of the Earth's core. *Earth and Planetary Science Letters*, *307*(3-4), 409–414.

Ono, S., & Kikegawa, T. (2006). High-pressure study of FeS, between 20 and 120 GPa, using synchrotron X-ray powder diffraction. *American Mineralogist*, *91*(11-12), 1941–

1944.

Pépin, C. M., Dewaele, A., Geneste, G., Loubeyre, P., & Mezouar, M. (2014). New iron hydrides under high pressure. *Physical Review Letters*, *113*(26), 265504.

Urakawa, S., Someya, K., Terasaki, H., Katsura, T., Yokoshi, S., Funakoshi, K.-i., ... Irifune, T. (2004). Phase relationships and equations of state for FeS at high pressures and temperatures and implications for the internal structure of Mars. *Physics of the Earth and Planetary Interiors*, *143*, 469–479.

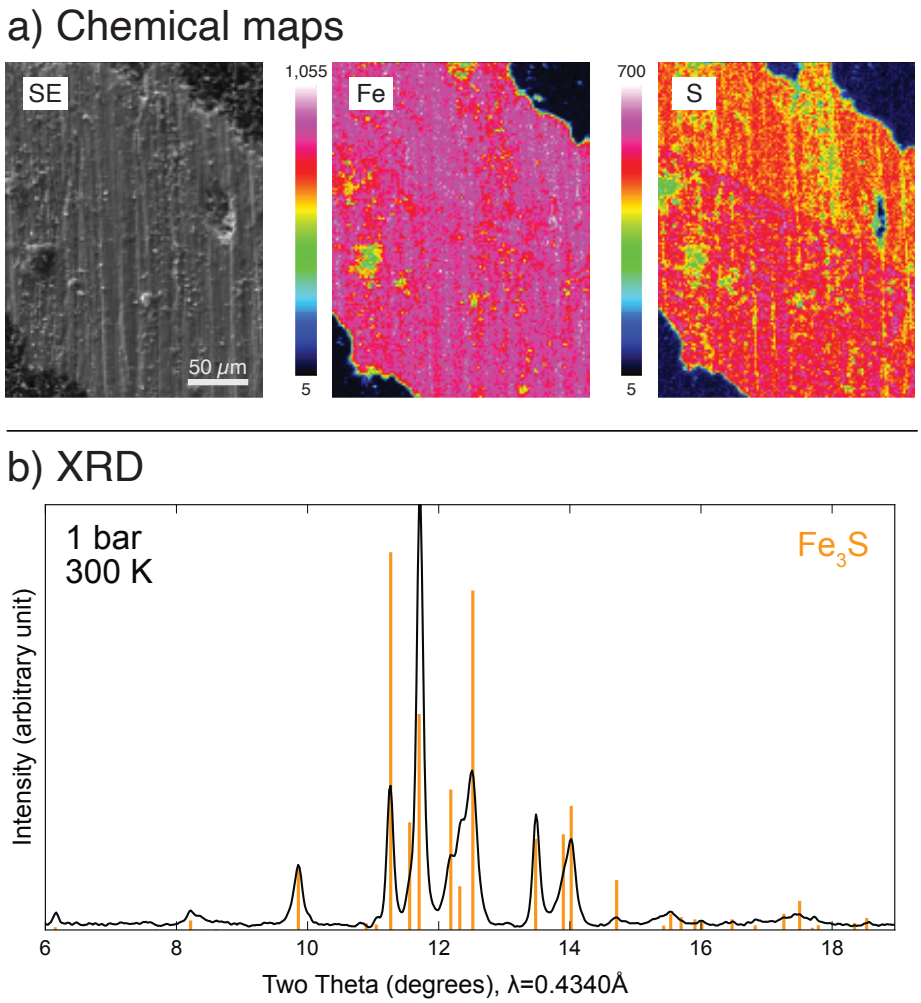

Figure S1. Scanning electron microscopy (SEM) and X-ray diffraction (XRD) data for pure Fe_3S synthesized in the multi-anvil press. (a) Secondary electron image and corresponding iron and sulfur WDS maps showing homogeneity of the sample for both chemical elements. Some areas with different colors in the compositional maps are from surface roughness of the unpolished cross sectional areas of the multi-anvil press sample. Point analyses in those areas yielded similar Fe and S compositions (Tab. S1). (b) XRD for this sample shows pure Fe_3S.

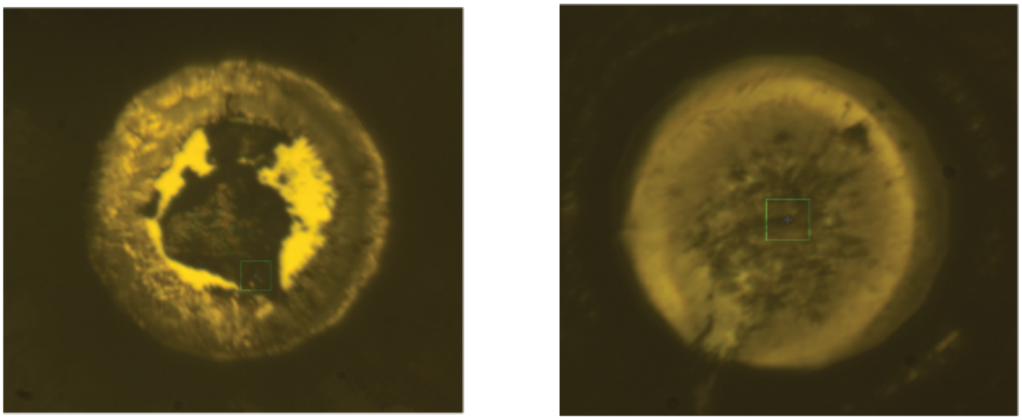

Figure S2. Difficulty in recovering the samples from LHDAC with a H_2 medium. The left photo shows hydrogen loaded sample at high pressure. The right photo shows sample collapse after decompression to 1 bar. We made particular care for very slow decompression, but the collapse is often difficult to prevent with H as a medium. The diameter of the cullet was 200 μm.

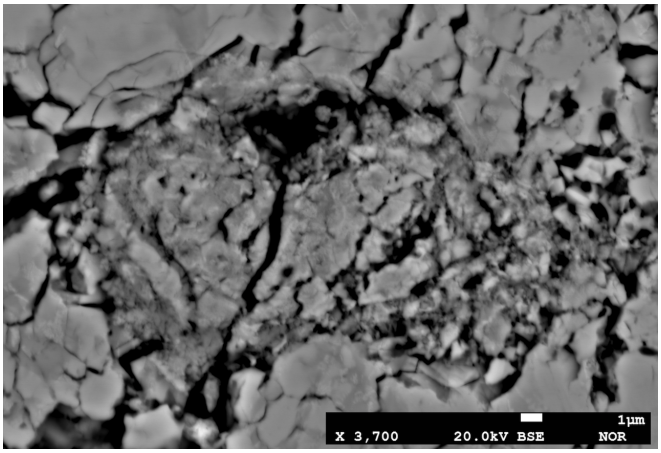

Figure S3. A backscattered electron image of the sample shown in Fig. 5. Even if Fe metal foils without micro-cracks are loaded initially, in a hydrogen medium, laser heating leads to significant developments of micro-cracks. The conversion of hydrogen from solid to liquid and then to gas during decompression for the recovery likely contributes to the development of micro-cracks as well.

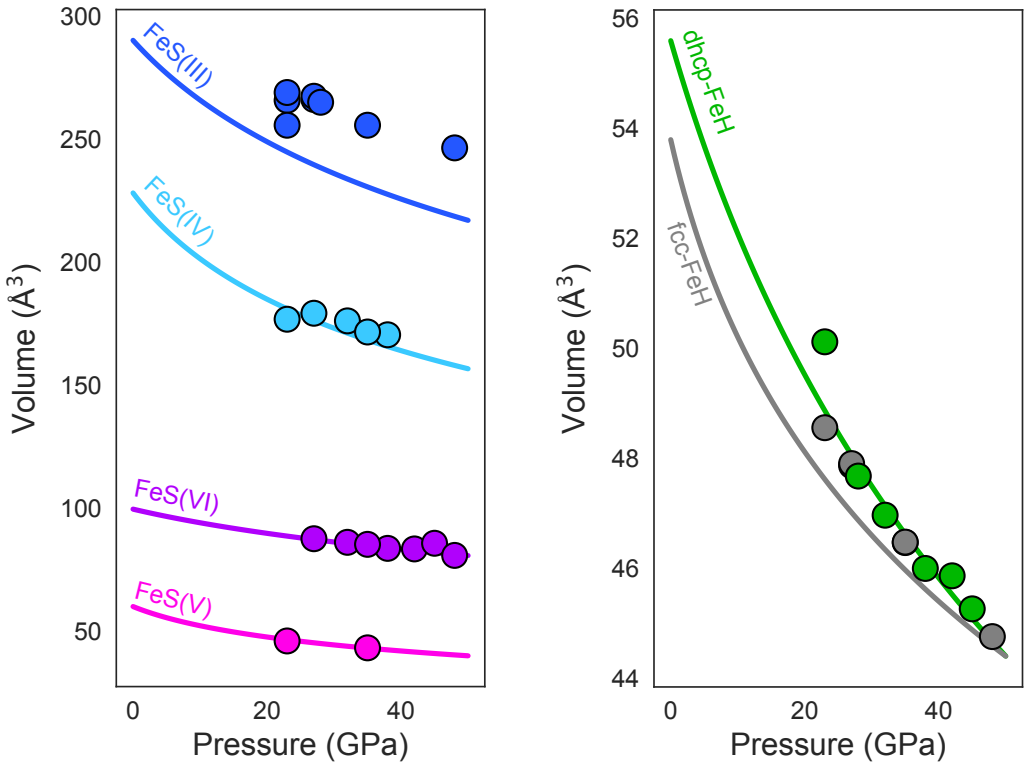

Figure S4. The unit-cell volumes of FeS(III), FeS(IV), FeS(V), FeS(VI), dhcp FeH_x, and fcc FeH_x laser-heated in a H medium in this study (the colored circles). The volumes were measured after laser heating at 300 K. The colored lines represent equations of state of the same phases from the literature. FeS(III): Kusaba et al. (1997); FeS(IV) and FeS(V): Urakawa et al. (2004); FeS(VI): Ono and Kikegawa (2006); dhcp FeH: Pépin et al. (2014); fcc FeH: Narygina et al. (2011). While FeS(VI) and FeS(V) did not show any sign of volume change when they were synthesized in a H medium, FeS(IV) and FeS(III) show increases in unit-cell volumes. Such increases suggest the presence of H in the crystal structures. The data points are provided in Tab. S7.

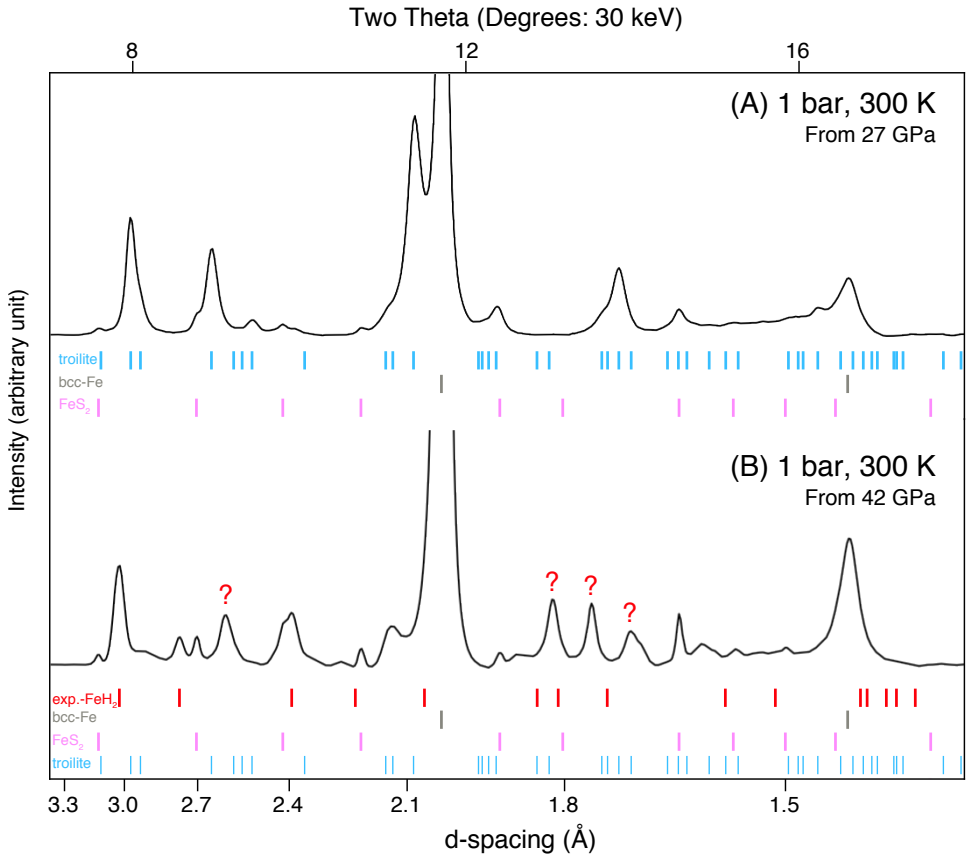

Figure S5. XRD diffraction patterns measured at 1 bar and 300 K after decompression. A) A Fe+Fe_3S mixture reacted with H at 27 GPa. Troilite (FeS(I)), bcc Fe, and FeS_2 are present. B) A Fe+Fe_3S mixture reacted with H at 42 GPa. Bcc Fe and FeS_2 are present, as well as some new diffraction lines.

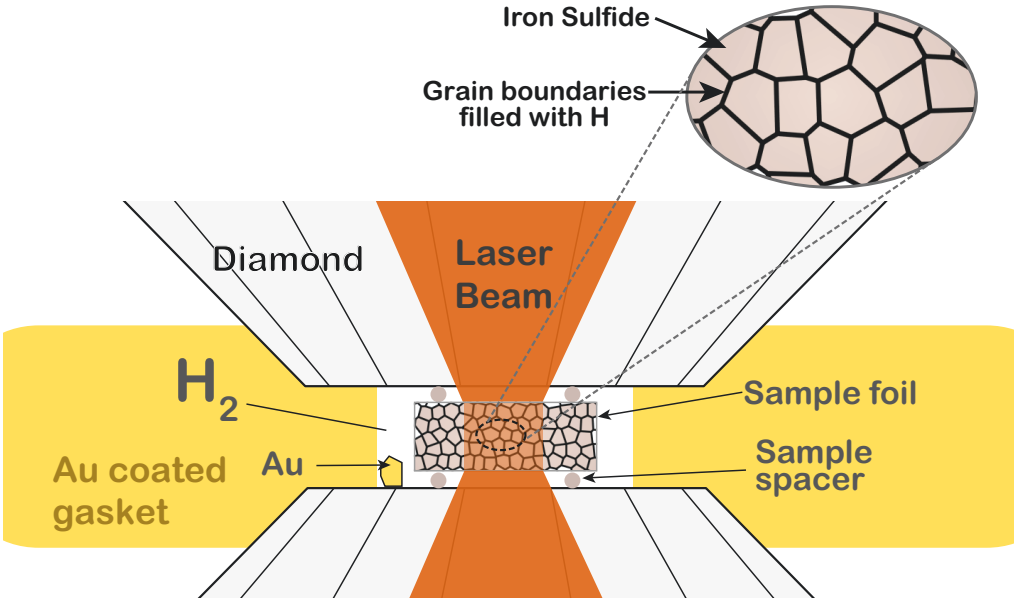

Figure S6. Schematic diagram for the sample configuration used in this study.

Table S1. Electron probe micro-analysis (EPMA) of the Fe_3S starting material (sample # BB1520) synthesized in the multi-anvil press (maximum temperature of 1533 K). Uncertainty (1σ) on the measurement is shown in parentheses. The data were obtained using wavelength-dispersive spectroscopy (WDS). See text for details about the samples and microprobe analysis procedure.

S (wt%)	Fe (wt%)	Total (wt%)
14.47(4)	84.99(11)	99.46
16.41(4)	83.27(10)	99.68

Table S2. Experimental runs. Uncertainties on the last digit(s) are shown in parenthesis.

SM: starting material; T_{range}: temperature range; P: pressure.

Run #	SM	P (GPa)	T_{range} (K)
231e	Fe_3S	28(2)	2820
331e	Fe_3S	32(2)	1930–2580
431e	Fe_3S	37(3)	3130–3950
120–220	Fe_3S	38(3)	1692–4057
320	Fe_3S	45(3)	2281–3076
132a	FeS	23(2)	1892–2272
103b	FeS	35(2)	1791–4579
131c	Fe+Fe_3S	27(2)	1150–2670
231c–431c	Fe+Fe_3S	42(3)	1520–4437

Table S3. Pressure-temperature conditions for the observation of the new FeS_xH_y ($x \approx 1$ and $y \approx 1$) phase. SM: starting material; P: pressure; T: temperature; $\sigma(P)$: 1σ uncertainty in pressure; $\sigma(T)$: 1σ uncertainty in temperature.

Run#	SM	P (GPa)	$\sigma(P)$ (GPa)	T (K)	$\sigma(T)$ (K)
120	Fe_3S	38	3	2572	150
220	Fe_3S	38	3	3340	702
220	Fe_3S	38	3	2462	201
220	Fe_3S	38	3	2882	419
220	Fe_3S	38	3	4057	150
220	Fe_3S	38	3	1692	347
320	Fe_3S	45	3	3076	150
320	Fe_3S	45	3	2342	153
320	Fe_3S	45	3	2281	228
320	Fe_3S	45	3	2480	250
320	Fe_3S	45	3	2593	391
231e	Fe_3S	28	2	2822	187
331e	Fe_3S	32	3	2575	150
331e	Fe_3S	32	3	1931	456
431e	Fe_3S	37	3	3458	274
431e	Fe_3S	37	3	3949	424
431e	Fe_3S	37	3	3126	150
131c	Fe+Fe_3S	27	2	1153	150
131c	Fe+Fe_3S	27	2	1701	382
131c	Fe+Fe_3S	27	2	1733	469
131c	Fe+Fe_3S	27	2	2406	484
131c	Fe+Fe_3S	27	2	2590	482
131c	Fe+Fe_3S	27	2	2551	292
131c	Fe+Fe_3S	27	2	2674	467
231c	Fe+Fe_3S	42	3	2040	150
231c	Fe+Fe_3S	42	3	1963	195
231c	Fe+Fe_3S	42	3	2336	153
231c	Fe+Fe_3S	42	3	2804	388
231c	Fe+Fe_3S	42	3	2763	150
231c	Fe+Fe_3S	42	3	2559	150
231c	Fe+Fe_3S	42	3	2848	804
231c	Fe+Fe_3S	42	3	2860	325
231c	Fe+Fe_3S	42	3	2616	519
231c	Fe+Fe_3S	42	3	3024	696
331c	Fe+Fe_3S	42	3	2851	431
431c	Fe+Fe_3S	42	3	2177	222
431c	Fe+Fe_3S	42	3	2266	529
431c	Fe+Fe_3S	42	3	3136	1400
431c	Fe+Fe_3S	42	3	1961	309
431c	Fe+Fe_3S	42	3	2346	498
431c	Fe+Fe_3S	42	3	4437	2922
431c	Fe+Fe_3S	42	3	1520	150
431c	Fe+Fe_3S	42	3	2985	531
431c	Fe+Fe_3S	42	3	2807	408
103b	FeS	35	2	3674	456
103b	FeS	35	2	1791	187
103b	FeS	35	2	3687	434
103b	FeS	35	2	4579	150
103b	FeS	35	2	2159	150
132a	FeS	23	2	2944	150
132a	FeS	23	2	2272	150
132a	FeS	23	2	2121	218
132a	FeS	23	2	2022	150
132a	FeS	23	2	1997	150
132a	FeS	23	2	1892	150
132a	FeS	23	2	2154	150
132a	FeS	23	2	2034	150
132a	FeS	23	2	2061	150
132a	FeS	23	2	2068	150
132a	FeS	23	2	2044	150
132a	FeS	23	2	2098	150

Table S4. X-ray diffraction data for the new phase (FeS_xH_y, $x \approx 1$ and $y \approx 1$) at 38 GPa. The data fitting to a tetragonal unit cell resulted in: $a = 2.979(3)$ Å and $c = 10.401(13)$ Å. hkl are Miller indices, 2θ is the Bragg diffraction angle and d is the d-spacing. obs: observed; calc: calculated; diff: difference.

h	k	l	2θ-obs (degrees)	d-obs (Å)	d-calc (Å)	d-diff (Å)
1	0	1	6.7034	2.8599	2.8617	−0.0018
0	0	4	7.3781	2.5986	2.6017	−0.0031
1	0	3	8.4880	2.2593	2.2589	0.0004
1	1	4	11.717	1.6380	1.6363	0.0017

Table S5. Unit-cell volumes of the new FeS_xH_y ($x \approx 1$ and $y \approx 1$) phase at high pressures. The volumes were measured at 300 K after high-temperature synthesis. P: pressure; V: unit-cell volume; $\sigma(P)$: 1σ uncertainty in pressure; $\sigma(V)$: 1σ uncertainty in unit-cell volume.

P (GPa)	$\sigma(P)$ (GPa)	V (Å^3)	$\sigma(V)$ (Å^3)
Run 231c			
0.0	0.0	109.36	0.11
3.5	0.1	107.70	0.11
5.7	0.2	106.45	0.11
11.1	0.3	103.82	0.10
13.8	0.4	103.37	0.10
16.2	0.5	101.12	0.10
19.7	0.6	99.13	0.10
23.2	0.7	97.65	0.10
26.9	0.8	95.16	0.10
33.1	1.0	93.03	0.09
39.6	1.2	92.37	0.09
40.3	1.2	91.76	0.09
42.3	1.3	91.83	0.09
Run 220			
0.2	0.0	109.54	0.11
1.4	0.0	108.58	0.11
3.0	0.1	107.04	0.11
4.1	0.1	106.41	0.11
14.9	0.4	103.21	0.10
19.5	0.6	101.06	0.10
21.9	0.7	100.13	0.10
23.9	0.7	98.79	0.10
25.2	0.8	98.06	0.10
27.6	0.8	98.03	0.10
30.2	0.9	97.19	0.10
33.5	1.0	95.19	0.10
37.4	1.1	93.34	0.09
38.7	1.2	93.22	0.09
41.3	1.2	91.98	0.09
44.5	1.3	91.06	0.09
45.4	1.4	90.83	0.09

Table S6. Volume difference between hcp-Fe (baseline) and different alloys (iron hydrides and iron sulfides). The corresponding volume increase caused by one atom of H was calculated and averaged over all Fe-rich alloys. The same analysis was performed for S. mol(H) or mol(S): # of H or S per Fe; ΔV(H) or ΔV(S): ΔV/(# of S or H per Fe).

Baseline	Alloy	ΔV (Å^3/Fe)	mol(H)	ΔV(H) (Å^3/Fe)
hcp-Fe	dhcp FeH	1.56	1.00	1.56
	FeH_2	3.82	2.00	1.91
	FeH_3	5.86	3.00	1.95
	FeH_5	10.05	5.00	2.01
Baseline	Alloy	ΔV (Å^3/Fe)	mol(S)	ΔV(S) (Å^3/Fe)
hcp-Fe	Fe_3S	2.89	0.33	8.66
	Fe_2S	4.22	0.50	8.43
	FeS	9.86	1.00	9.86
	FeS_2	21.46	2.00	10.73

Table S7. Unit-cell volumes of the main phases synthesized in a H medium in this study at high pressures and high temperatures. The volumes were measured at 300 K after synthesis. SM: starting material; P: pressure; V: unit-cell volume; $\sigma(P)$: 1σ uncertainty in pressure; $\sigma(V)$: 1σ uncertainty in unit-cell volume.

SM	P (GPa)	$\sigma(P)$ (GPa)	V (Å^3)	$\sigma(V)$ (Å^3)
		dhcp FeH_x		
Fe+Fe_3S	27	2	47.86	0.02
Fe+Fe_3S	42	3	45.86	0.02
Fe_3S	28	2	47.67	0.02
Fe_3S	32	2	46.96	0.02
Fe_3S	38	3	45.99	0.02
Fe_3S	45	3	45.26	0.02
FeS	23	2	50.12	0.03
FeS	35	2	46.46	0.02
		fcc FeH_x		
Fe+Fe_3S	27	2	47.90	0.02
FeS	23	2	48.55	0.02
FeS	35	2	46.47	0.02
FeS	48	3	44.75	0.02
		FeS(III)		
Fe+Fe_3S	27	2	265.98	0.13
Fe+Fe_3S	27	2	267.29	0.13
Fe_3S	28	2	264.85	0.13
FeS	23	2	265.62	0.13
FeS	23	2	255.52	0.13
FeS	23	2	268.81	0.13
FeS	35	2	255.52	0.13
FeS	48	3	246.31	0.12
		FeS(IV)		
Fe+Fe_3S	27	2	179.11	0.09
Fe_3S	32	2	176.00	0.09
Fe_3S	38	3	170.35	0.09
FeS	23	2	176.68	0.09
FeS	35	2	171.49	0.09
		FeS(V)		
FeS	35	2	43.13	0.02
FeS	23	2	45.55	0.02
		FeS(VI)		
Fe+Fe_3S	27	2	87.47	0.04
Fe+Fe_3S	42	3	83.33	0.04
Fe_3S	32	2	86.01	0.04
Fe_3S	38	3	83.55	0.04
Fe_3S	45	3	85.63	0.04
FeS	35	2	85.19	0.04
FeS	48	3	80.70	0.04